

Chapter 13

Neutrino Scattering from Hadrons: Deep Inelastic Scattering

13.1 Introduction

In 1951, Lyman, Hanson, and Scott [541] were the first to observe elastic electron scattering from different nuclei using a 15.7 MeV beam obtained with the help of the betatron accelerator facility at Illinois. Further extensive studies using electron beams started with the development of the Mark III linear accelerator (LINAC) in 1953 at the High Energy Physics Laboratory (HEPL), Stanford. Hofstadter, Fechter, and McIntyre studied the effect of electron scattering ($E_e \sim 125 - 150$ MeV) on various nuclear targets and concluded that these nuclei have finite charge distribution. With increased energy (550 MeV) available for scattering, the first evidence of elastic scattering from the proton was observed by Chambers and Hofstadter at HEPL in 1956 [542], using a polyethylene target. Assuming that proton had an exponential density distribution, they found the r.m.s. (root mean squared) radius of the proton to be about 0.8 fm. Later, Yearian and Hofstadter performed electron scattering experiments on deuteron targets and determined the magnetic moment of the neutron [543]. At that time, the investigation of the structure of the proton and neutron was a major objective of HEPL, which was upgraded to achieve electron beams of energies up to 20 GeV; today, HEPL is known as the Stanford Linear Accelerator Center (SLAC) [544]. By the 1960s, it became possible to perform both elastic and inelastic scattering experiments at high energies and for a wide range of four-momentum transfer squared (Q^2). Thus, by the end of the 1960s, nuclear physics entered the ‘deep inelastic scattering’ (DIS) era, when experiments with 20–40 times higher energies were being performed at SLAC; it became possible to probe the hadron. DIS is the scattering of charged leptons/neutrinos from hadrons in the kinematic region of very high Q^2 and energy transfer ν . During the late 1960s, experiments by MIT-SLAC collaboration, led by Taylor, Kendall, and Friedman [544] confirmed the scaling phenomenon in the deep inelastic region, which was theoretically predicted by Bjorken [545, 546]. They received the 1990 Nobel

Prize in Physics for the experiments. These experimental results confirmed that, in the scaling region, the constituents of protons behave like free particles called partons. Charged partons are identified as quarks and neutral partons are identified as gluons. Later, many experiments using electron and muon beams were performed at CERN, DESY, Fermilab, etc. and their results were consistent with the earlier observations. In fact, Bjorken predicted that if neutrino beams are used in the DIS (deep inelastic scattering) region, then scaling should also be observed in the case of weak interactions [546]; this was indeed observed in the experiments performed at CERN using deuteron targets. Today, we understand nucleons to be composite systems of quarks and gluons with many internal degrees of freedom. The quantum field theory of quarks and gluons is known as quantum chromodynamics (QCD) which is a non-abelian gauge theory, with symmetry group $SU(3)_C$ in color space. These developments can be better understood

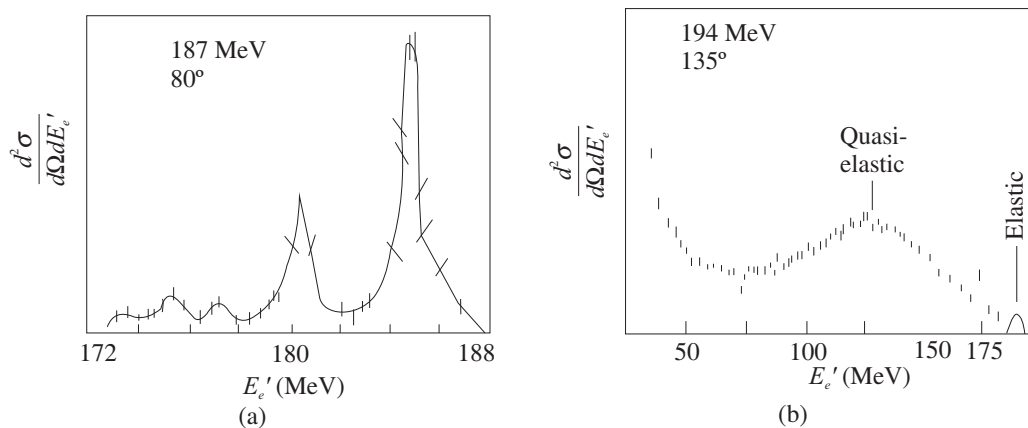


Figure 13.1 $e^- - {}^{12}\text{C}$ scattering cross section (a) $\theta = 80^\circ$, $Q^2 \rightarrow 0.06 \text{ GeV}^2$. The elastic peak is evident at low energy transfer; the excitation of nuclear levels can be seen with increase in energy transfer. (b) $\theta = 135^\circ$, $Q^2 \sim 0.1 \text{ GeV}^2$. The large, broad peak between 100 and 150 MeV is due to quasielastic scattering from individual neutrons and protons that make up the carbon nucleus [425].

with the help of Figures 13.1, 13.2, and 13.3. In Figure 13.1(a), the differential scattering cross section for elastic $e^- - {}^{12}\text{C}$ scattering at low Q^2 has been shown. The peak of the elastic scattering cross section may be seen for an electron of incident energy $E_e = 190 \text{ MeV}$, lab scattering angle $\theta = 80^\circ$, and the outgoing electron's energy $E_e' = 187 \text{ MeV}$, which corresponds to $Q^2 \simeq 0.06 \text{ GeV}^2$. With the increase in the energy transfer, that is, $E_e - E_e'$, nuclear excitations may be observed. The observation of nuclear excitations or, in general, hadron excitations imply that the object has a composite structure. At higher Q^2 , corresponding to higher scattering angle, the elastic peak gets suppressed and a quasielastic peak is observed which corresponds to the scattering from individual nucleons. For example, in Figure 13.1(b), at $\theta = 135^\circ$, $Q^2 \sim 0.1 \text{ GeV}^2$, one may notice that the elastic scattering is suppressed and the broad peak between 100 and 150 MeV, which is due to the quasielastic scattering from individual neutrons and protons that make up the carbon nucleus, becomes prominent. This peak is smeared because the nucleons inside the nucleus are bound and moving with a finite momenta.

The phenomenon may also be understood in terms of the Bjorken variable x , which is defined as

$$x = -\frac{q^2}{2p \cdot q} \left(= \frac{Q^2}{2M\nu} \text{ in lab frame} \right), \quad (13.1)$$

where M is the nucleon mass and $\nu = E_l - E_l'$ is the energy transferred to the target particle. $Q^2 = -q^2 \simeq 4E_l E_l' \sin^2 \left(\frac{\theta}{2} \right) \geq 0$ in the limit $m_l \rightarrow 0$, x lies between 0 and 1 and is equal to 1 for an elastic scattering process as shown below.

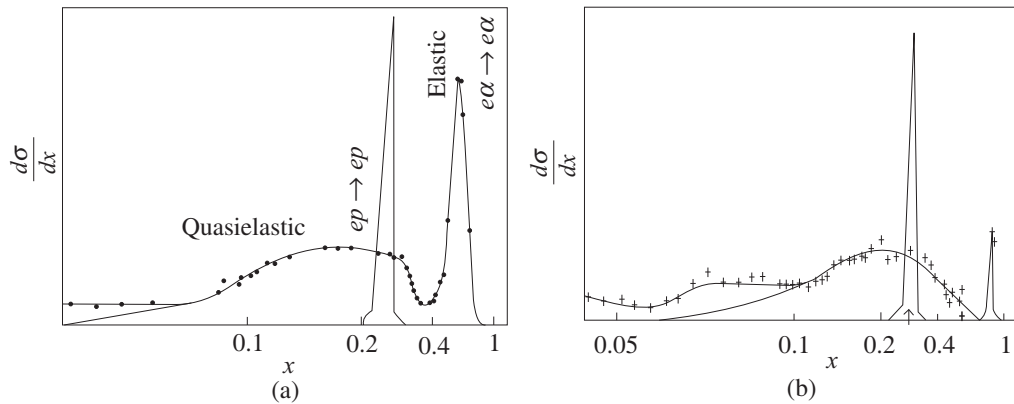


Figure 13.2 $e^- - {}^4\text{He}$ scattering cross section for the beam energy $E_e = 400$ MeV (a) Left: $\theta = 45^\circ$, $Q^2 \rightarrow 0.08$ GeV², (b) Right: $\theta = 60^\circ$, $Q^2 \rightarrow 0.1$ GeV² [425].

Let us now consider the process $e^-(k) + p(p) \rightarrow e^-(k') + N^*(p')$, where N^* may be a proton (elastic), or a Δ (resonance excitation). Using the definition of invariant mass square (W^2),

$$\begin{aligned} W^2 &= p'^2 = (p + q)^2 = p^2 + q^2 + 2p \cdot q, \text{ where } q = k - k' = p' - p, \\ \Rightarrow W &= \sqrt{s} = \sqrt{M^2 + q^2 + 2M(E_l - E_l')}. \end{aligned}$$

For an elastic scattering process, $W = M$ and the aforementioned equation reduces to $q^2 = -2M(E_l - E_l')$. From Eq. (13.1), one may obtain $x = 1$ for the elastic scattering process and the corresponding peak in the cross section was observed. For example, in the case of elastic scattering of electrons off α particles, there is a peak at $x \sim 1$, at low Q^2 (Figure 13.2(a)); with increase in Q^2 , the quasielastic peak appears which is diminished and broad. This represents the fact that there are subnuclear objects inside the helium nucleus. Had these nucleons been free particles at rest, the peak would have occurred at $x = \frac{1}{4}$ (corresponding to the two neutrons and two protons). The smeared peak implies that these nucleons are neither free nor static. With further increase in Q^2 , the elastic peak gets suppressed and gradually with the decrease in x , the quasielastic peak becomes almost Q^2 independent. In general, one would expect that as $x \rightarrow 0$, the quasielastic peak should die away, whereas, in Figure 13.2(b), it may be observed that it is not the case. A finite value of the cross section represents the fact that as $x \rightarrow 0$,

there are subnuclear objects other than nucleons from which e^- scattering is taking place; the scattering is understood to be the interaction of electrons with pions, rho mesons, etc. arising due to nucleon–nucleon interaction.

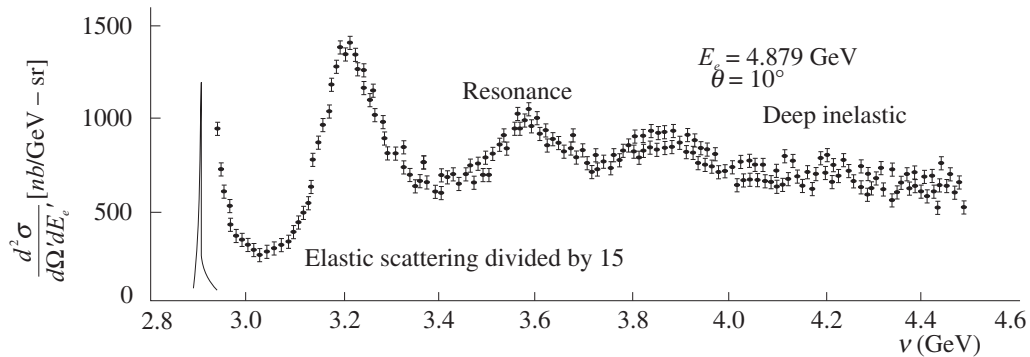


Figure 13.3 Electron–proton double differential scattering cross sections at $E_e = 4.879$ MeV; lab scattering angle $\theta = 10^\circ$. The X-axis represents the energy transferred to the target proton ($\nu = E_e - E'_e$). The elastic peak (solid curve) has been divided by a factor of 15 to present the curves on the same scale [547].

Similarly, in the case of elastic electron scattering from the proton target (Figure 13.3), the peak is observed at low energy transfer or equivalently when the invariant mass $W \sim M$. Recall from Chapter 10, that the structure of the proton is described in terms of the electric and magnetic Sachs form factors; the size of the proton and its magnetic moment may also be understood with the help of these form factors. The Q^2 dependence of the form factors implies that the elastic cross section decreases with the increase in four-momentum transfer squared. In fact, with the increase in Q^2 , the proton form factors decrease almost by two orders of magnitude in the Q^2 range of $1 < Q^2 < 10 \text{ GeV}^2$. With increase in energy transfer, one observes inelastic scattering which results in the production of one pion, multipions, etc. for which $W > M$. For large energy transfer, resonant states are formed, which indeed have been experimentally observed.

Now the question arises, what happens when Q^2 becomes very large? At high Q^2 , the proton breaks up into a jet of hadrons (shown in Figure 13.4 (c)) and the final state is now a multiparticle state with large invariant mass. In contrast to the rapid fall of elastic proton form factors with increase in Q^2 , the proton structure functions in the case of deep inelastic scattering process was observed to be independent of Q^2 and ν in the limit $Q^2 \rightarrow \infty, \nu \rightarrow \infty$ at a fixed value of x (true for a wide range of x). Thus, the cross section scales and the structure functions depend only on a single dimensionless variable, $\omega = \frac{1}{x} = \frac{2M\nu}{Q^2}$. This phenomenon is known as Bjorken scaling.

In this chapter, the general formalism for the charged lepton–nucleon DIS process is discussed in Section 13.2. In Subsection 13.2.1, a discussion on the Bjorken scaling and the Callan–Gross relation is given. Then, in Sections 13.3 and 13.4, this formalism is applied to describe the (anti)neutrino–nucleon charged and neutral current DIS processes following some discussion in Section 13.5 on non-perturbative and perturbative effects that modulate

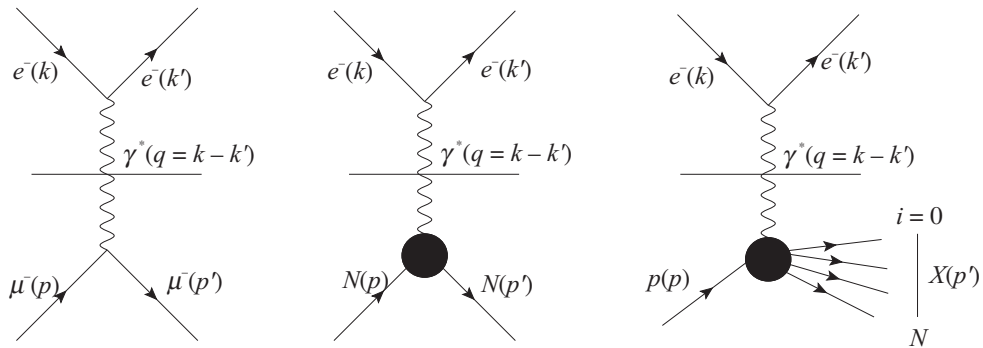


Figure 13.4 (a) Left: electron–muon scattering (b) Center: electron–proton elastic scattering, and (c) Right: electron–proton deep inelastic scattering.

the structure functions. After that, in Section 13.6, the parton model sum rules involving electromagnetic and weak structure functions have been discussed. The last section of this chapter deals with the phenomenon of quark–hadron duality.

13.2 Charged Lepton–nucleon DIS

The general reaction for the deep inelastic scattering process is given by (Figure 13.4(c))

$$l^-(k) + N(p) \longrightarrow l^-(k') + X(p'), \quad (13.2)$$

where $l = e, \mu$, $N = n, p$, and X represents the jet of hadrons in the final state.

To evaluate the differential scattering cross section for the process given in Eq. (13.2), the same method has been followed as discussed in Chapter 9 for $e^- \mu^- \rightarrow e^- \mu^-$ or in Chapter 10 for $e^- p \rightarrow e^- p$ scattering processes. We can notice that in all the three Feynman diagrams shown in Figure 13.4, the source of virtual photon is an electron (above the dashed line), which gets absorbed by a muon (scenario shown in Figure 13.4(a)), or a proton (scenario shown in Figure 13.4(b)) or it breaks the proton into a jet of hadrons (scenario shown in Figure 13.4(c)). Therefore, the leptonic current contributing to all the three processes (above the dashed line in Figure 13.4 (a), (b) and (c)) are the same. The differential scattering cross section can be expressed in terms of $\overline{\sum} \sum |\mathcal{M}|^2$ as

$$d\sigma \propto \overline{\sum} \sum |\mathcal{M}|^2, \quad (13.3)$$

which consists of the leptonic tensor,

$$L_{\mu\nu} = 4(k_\mu k'_\nu - g_{\mu\nu} k \cdot k' + k_\nu k'_\mu + m_l^2 g_{\mu\nu}), \quad (13.4)$$

and a muonic (Figure 13.4(a)) or a hadronic (Figure 13.4(b) or (c)) tensor $W_N^{\mu\nu}$. Since $\overline{\sum} \sum |\mathcal{M}|^2$ has to be a Lorentz invariant quantity, the hadronic vertex should also be a second rank tensor similar to the leptonic vertex tensor. A tensor of rank two for the lower vertex is formed by

using muonic current (Chapter 9) in the case of electron–muon scattering and proton current (Chapter 10) in the case of electron–proton elastic scattering processes.

For DIS, the final state hadrons are not observed and therefore, one cannot write down the expression for the hadronic current. For example, for the inclusive charged lepton–nucleon DIS process, which is depicted in Figure 13.5, one must sum over the final hadronic states X and write down the general expression of the second rank hadronic tensor ($W_N^{\mu\nu}$) by using the

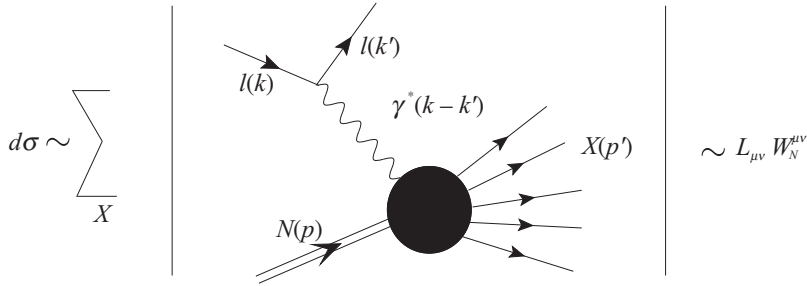


Figure 13.5 Charged lepton–nucleon inclusive scattering process.

bilinear covariants discussed in Chapter 4, along with p and q , the available four momenta. All possible combinations of tensors with four momenta p , q , and the metric tensor $g_{\mu\nu}$ at the hadronic vertex are the following

$$g^{\mu\nu}, p^\mu p^\nu, q^\mu q^\nu, \epsilon^{\mu\nu\lambda\sigma} p_\lambda q_\sigma, p^\mu q^\nu + p^\nu q^\mu, p^\mu q^\nu - p^\nu q^\mu,$$

using, which the most general form of the nucleon hadronic tensor is written as

$$\begin{aligned} W_N^{\mu\nu} = & -g^{\mu\nu} W_{1N}^{\text{EM}}(\nu, Q^2) + \frac{p^\mu p^\nu}{M^2} W_{2N}^{\text{EM}}(\nu, Q^2) \\ & -i\epsilon^{\mu\nu\lambda\sigma} \frac{p_\lambda q_\sigma}{2M^2} W_{3N}^{\text{EM}}(\nu, Q^2) + \frac{q^\mu q^\nu}{M^2} W_{4N}^{\text{EM}}(\nu, Q^2) \\ & + \frac{(p^\mu q^\nu + p^\nu q^\mu)}{M^2} W_{5N}^{\text{EM}}(\nu, Q^2) + i \frac{(p^\mu q^\nu - p^\nu q^\mu)}{M^2} W_{6N}^{\text{EM}}(\nu, Q^2), \end{aligned} \quad (13.5)$$

where M is the mass of the target nucleon. The nucleon structure functions $W_{iN}^{\text{EM}}(\nu, Q^2)$, ($i = 1 - 6$) are the functions of ν and Q^2 . $W_{3N}^{\text{EM}}(\nu, Q^2)$ arises due to parity violation; therefore, it would not contribute in the electromagnetic interaction processes. Furthermore, the antisymmetric term that is related to $W_{6N}^{\text{EM}}(\nu, Q^2)$ vanishes when contracted with the leptonic tensor, which has symmetric terms only. The conservation of vector current (CVC) at the hadronic vertex implies

$$q_\nu W_N^{\mu\nu} = q_\mu W_N^{\mu\nu} = 0,$$

which leads to the following relations

$$\left. \begin{aligned} W_{4N}^{\text{EM}}(\nu, Q^2) &= \frac{M^2}{q^2} W_{1N}^{\text{EM}}(\nu, Q^2) + \left(\frac{p \cdot q}{q^2}\right)^2 W_{2N}^{\text{EM}}(\nu, Q^2), \\ W_{5N}^{\text{EM}}(\nu, Q^2) &= \frac{-p \cdot q}{q^2} W_{2N}^{\text{EM}}(\nu, Q^2). \end{aligned} \right\} \quad (13.6)$$

Thus, we are left with only two independent structure functions, which are generally chosen to be $W_{1N}^{\text{EM}}(\nu, Q^2)$ and $W_{2N}^{\text{EM}}(\nu, Q^2)$. The expression of $W_N^{\mu\nu}$ is written in terms of these two structure functions as:

$$W_N^{\mu\nu} = \left(\frac{q^\mu q^\nu}{q^2} - g^{\mu\nu}\right) W_{1N}^{\text{EM}}(\nu, Q^2) + \left(p^\mu - \frac{p \cdot q}{q^2} q^\mu\right) \left(p^\nu - \frac{p \cdot q}{q^2} q^\nu\right) \frac{W_{2N}^{\text{EM}}(\nu, Q^2)}{M^2}. \quad (13.7)$$

Contraction of $L_{\mu\nu}$ with $W_N^{\mu\nu}$ leads to the following expression

$$\begin{aligned} L_{\mu\nu} W_N^{\mu\nu} &= 4W_{1N}^{\text{EM}}(\nu, Q^2) \left\{ -2k \cdot k' + 4(k \cdot k' - m_l^2) + 2\frac{q \cdot k q \cdot k'}{q^2} - (k \cdot k' - m_l^2) \right\} \\ &+ \frac{4W_{2N}^{\text{EM}}(\nu, Q^2)}{M^2} \left\{ 2p \cdot k p \cdot k' - M^2(k \cdot k' - m_l^2) + \left(\frac{p \cdot q}{q^2}\right)^2 \right. \\ &\times \left\{ 2q \cdot k q \cdot k' - (k \cdot k' - m_l^2) q^2 \right\} - \left(\frac{p \cdot q}{q^2}\right) \{ 2p \cdot k q \cdot k' + 2q \cdot k p \cdot k' \\ &\left. - 2(k \cdot k' - m_l^2) p \cdot q \} \right\}. \end{aligned} \quad (13.8)$$

In the limit of the massless lepton, Eq. (13.8) reduces to the following form:

$$L_{\mu\nu} W^{\mu\nu} = 4W_{1N}^{\text{EM}}(\nu, Q^2) [-q^2] + 4\frac{W_{2N}^{\text{EM}}(\nu, Q^2)}{M^2} [2p \cdot k p \cdot k' - M^2 k \cdot k']. \quad (13.9)$$

Averaging over the initial electron's and nucleon's spins and taking a sum over the final electron's and nucleon's spins, one gets the expression of $\overline{\sum} \sum |\mathcal{M}|^2$ in the Lab frame as:

$$\overline{\sum} \sum |\mathcal{M}|^2 = \frac{e^4}{q^4} L_{\mu\nu} W^{\mu\nu} = \frac{e^4}{q^4} 2E_l E_l' \left\{ 2\sin^2\left(\frac{\theta}{2}\right) W_{1N}^{\text{EM}}(\nu, Q^2) + \cos^2\left(\frac{\theta}{2}\right) W_{2N}^{\text{EM}}(\nu, Q^2) \right\}, \quad (13.10)$$

where θ is the Lab scattering angle between an incoming and an outgoing charged lepton.

To get the expression of the differential scattering cross section in the Lab frame, let us start with the general expression for the scattering cross section for a two-body scattering process; for example, $e^-(k) + p(p) \rightarrow e^-(k') + X(p')$:

$$d\sigma = \frac{1}{4\sqrt{(p \cdot k)^2 - m_l^2 M^2}} \overline{\sum} \sum |\mathcal{M}|^2 \cdot \frac{d^3 k'}{(2\pi)^3 2E_l'} \cdot \frac{d^3 p'}{(2\pi)^3 2E_X} (2\pi)^4 \delta^4(p' + k' - p - k) \quad (13.11)$$

which simplifies to

$$d\sigma = \frac{1}{4ME_l} \bar{\Sigma} \Sigma |\mathcal{M}|^2 \frac{1}{4\pi^2} \delta^4(p' + k' - p - k) \frac{d^3 p'}{2E_X} \frac{d^3 k'}{2E_l'} \quad (13.12)$$

Performing momentum integration over $d^3 p'$ results in:

$$d\sigma = \frac{1}{4ME_l} \bar{\Sigma} \Sigma |\mathcal{M}|^2 \frac{1}{4\pi^2} \delta^0(E_X + E_l' - E_l - M) \frac{1}{2E_X} \frac{|\vec{k}'|^2 d|\vec{k}'| d\Omega_l'}{2E_l'} \quad (13.13)$$

$$\Rightarrow \frac{d^2\sigma}{d\Omega_l' dE_l'} = \frac{1}{4ME_l} \bar{\Sigma} \Sigma |\mathcal{M}|^2 \frac{1}{4\pi^2} \delta^0(E_X + E_l' - E_l - M) \frac{E_l'}{4E_X} \quad (13.14)$$

Using the expression of $\bar{\Sigma} \Sigma |\mathcal{M}|^2$ from Eq. (13.10), the differential scattering cross section is then given by

$$\begin{aligned} \frac{d^2\sigma}{d\Omega_l' dE_l'} &= \frac{1}{4ME_l} \frac{e^4}{q^4} 2E_l E_l' \left\{ 2 \sin^2 \left(\frac{\theta}{2} \right) W_{1N}^{\text{EM}}(\nu, Q^2) + \cos^2 \left(\frac{\theta}{2} \right) W_{2N}^{\text{EM}}(\nu, Q^2) \right\} \frac{1}{4\pi^2} \\ &\quad \times \delta^0(E_X + E_l' - E_l - M) \frac{E_l'}{4} \frac{1}{M} \frac{M}{E_X}. \end{aligned} \quad (13.15)$$

The structure functions $W_{1N}^{\text{EM}}(\nu, Q^2)$ and $W_{2N}^{\text{EM}}(\nu, Q^2)$ are redefined as

$$W_{1N}^{\text{EM}}(\nu, Q^2) \left\{ \frac{1}{8M} \frac{1}{E_X} \right\} \delta^0(E_X + E_l' - E_l - M) \rightarrow W_{1N}^{\text{EM}}(\nu, Q^2), \quad (13.16)$$

$$W_{2N}^{\text{EM}}(\nu, Q^2) \left\{ \frac{1}{8M} \frac{1}{E_X} \right\} \delta^0(E_X + E_l' - E_l - M) \rightarrow W_{2N}^{\text{EM}}(\nu, Q^2). \quad (13.17)$$

Keeping the same name is just a choice.

This results in the following expression for inclusive differential scattering cross section

$$\frac{d^2\sigma}{d\Omega_l' dE_l'} = \frac{\alpha^2}{4E_l^2 \sin^4 \left(\frac{\theta}{2} \right)} \left\{ 2 \sin^2 \left(\frac{\theta}{2} \right) W_{1N}^{\text{EM}}(\nu, Q^2) + \cos^2 \left(\frac{\theta}{2} \right) W_{2N}^{\text{EM}}(\nu, Q^2) \right\}, \quad (13.18)$$

which can equivalently be also expressed in terms of Q^2 and ν distributions, that is, $\frac{d^2\sigma}{dQ^2 d\nu}$. This is obtained using the following relation:

$$\frac{d^2\sigma}{dQ^2 d\nu} = \frac{\pi}{E_l E_l'} \frac{d^2\sigma}{d\Omega_l' dE_l'} \quad (13.19)$$

resulting in

$$\frac{d^2\sigma}{dQ^2 d\nu} = \frac{\pi \alpha^2}{4E_l^3 E_l' \sin^4 \left(\frac{\theta}{2} \right)} \left\{ 2 \sin^2 \left(\frac{\theta}{2} \right) W_{1N}^{\text{EM}}(\nu, Q^2) + \cos^2 \left(\frac{\theta}{2} \right) W_{2N}^{\text{EM}}(\nu, Q^2) \right\} \quad (13.20)$$

13.2.1 Bjorken scaling and parton model

In elastic $e^- - p$ scattering (Chapter 10), if one assumes $G_E(Q^2) = G_M(Q^2) = G(Q^2)$, where $G(Q^2) = \frac{1}{(1 + \frac{Q^2}{M_V^2})^2}$ with M_V as the vector dipole mass, then the expression of the

differential scattering cross section may be expressed as:

$$\frac{d^2\sigma}{d\Omega'_l dE'_l} = \frac{\alpha^2 G(Q^2)}{4E_l^2 \sin^4(\frac{\theta}{2})} \left\{ \cos^2\left(\frac{\theta}{2}\right) + \frac{Q^2}{2M^2} \sin^2\left(\frac{\theta}{2}\right) \right\} \delta\left(\nu - \frac{Q^2}{2M}\right). \quad (13.21)$$

It may be noticed that for the elastic $e^- - p$ scattering process, the form factors depend explicitly on Q^2 and an explicit mass scale (M_V) is present. However, if the proton is considered to be a point particle, that is, $G(Q^2) = 1$ and $M = m$ (mass of a point particle), then Eq. (13.21) gets modified to:

$$\frac{d^2\sigma}{d\Omega'_l dE'_l} = \frac{\alpha^2}{4E_l^2 \sin^4(\frac{\theta}{2})} \left\{ \cos^2\left(\frac{\theta}{2}\right) + \frac{Q^2}{2m^2} \sin^2\left(\frac{\theta}{2}\right) \right\} \delta\left(\nu - \frac{Q^2}{2m}\right), \quad (13.22)$$

which is the same as the differential cross section for $e\mu \rightarrow e\mu$ scattering process (Chapter 9). Comparing Eqs. (13.18) and (13.22), we may write in the limits of high ν and Q^2 :

$$\left. \begin{aligned} \nu W_2^{\text{point}}(\nu, Q^2) &= \delta\left(1 - \frac{Q^2}{2m\nu}\right), \\ 2mW_1^{\text{point}}(\nu, Q^2) &= \frac{Q^2}{2m\nu} \delta\left(1 - \frac{Q^2}{2m\nu}\right), \end{aligned} \right\} \quad (13.23)$$

where the identity $\delta\left(\nu - \frac{Q^2}{2m}\right) = \frac{1}{\nu} \delta\left(1 - \frac{Q^2}{2m\nu}\right)$ has been used. The aforementioned expressions show that for point particles (Figure 13.6), the structure functions are functions of one variable, $\frac{Q^2}{2m\nu}$, and not independent functions of Q^2 and ν (see Figure 13.7). In 1969,

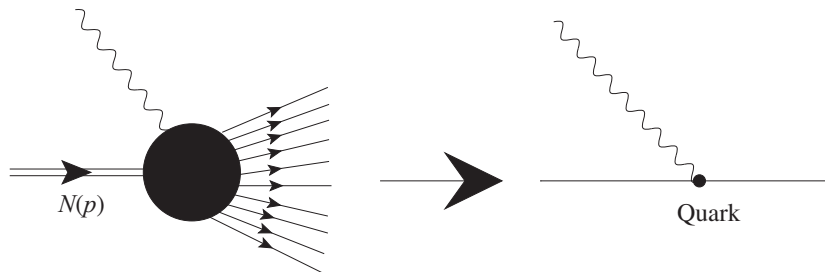


Figure 13.6 Left: A virtual photon interacting with a hadron; Right: A virtual photon interacting with a point Dirac particle inside a hadron.

Bjorken had proposed that in the region of high ν and Q^2 ($\nu \rightarrow \infty$, $Q^2 \rightarrow \infty$), the structure functions $W_1(\nu, Q^2)$ and $W_2(\nu, Q^2)$ would only depend upon the ratio $\frac{Q^2}{\nu} (\sim x)$. To introduce

the structure functions as a function of a single dimensionless variable $\omega = \frac{1}{x} = \frac{2M\nu}{Q^2}$, $W_1(\nu, Q^2)$ and $W_2(\nu, Q^2)$ are redefined as:

$$\left. \begin{aligned} \nu W_2(\nu, Q^2) &= F_2(x), \\ MW_1(\nu, Q^2) &= F_1(x). \end{aligned} \right\} \quad (13.24)$$

In the case of DIS, the early results by Friedman and Kendall at SLAC [544] also showed that the results for $\frac{d^2\sigma}{d\Omega'_l dE'_l}$ in the region of high Q^2 and ν seem to depend only on one variable, that is, $\frac{Q^2}{2M\nu}$. This implies that in this kinematic limit, the cross section scales.

Now the scattering cross section given in Eq. (13.18) may be expressed in terms of the dimensionless nucleon structure functions as:

$$\frac{d^2\sigma}{d\Omega'_l dE'_l} = \frac{\alpha^2}{4M\nu E_l^2 \sin^4\left(\frac{\theta}{2}\right)} \left\{ 2 \sin^2\left(\frac{\theta}{2}\right) \nu F_{1N}^{\text{EM}}(x) + \cos^2\left(\frac{\theta}{2}\right) MF_{2N}^{\text{EM}}(x) \right\}. \quad (13.25)$$

The phenomenon of scaling, that is, the dependence of $\frac{d^2\sigma}{d\Omega'_l dE'_l}$ on a single variable x suggests that in this limit of high Q^2 and ν , the deep inelastic electrons scattering from the constituents of the proton can be treated as point particles and the DIS cross section should be treated as the incoherent sum of elastic scattering from point-like constituents of the proton, as suggested by Bjorken. These constituents are called partons. The signature that the structure functions are now independent of Q^2 or ν may be realized by plotting $MW_{1N}^{\text{EM}}(\nu, Q^2)$ vs. Q^2 (or equivalently

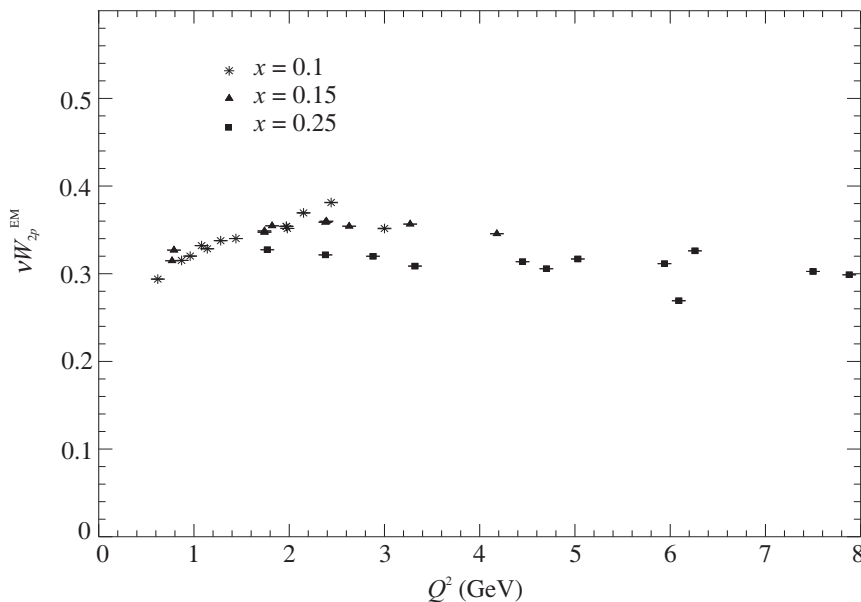


Figure 13.7 $\nu W_{2p}^{\text{EM}}(\nu, Q^2)$ vs. Q^2 at a fixed $x = \frac{1}{\omega}$. Experimental data are from SLAC [548].

ν); or $\nu W_{2N}^{\text{EM}}(\nu, Q^2)$ vs. Q^2 (or equivalently ν), at a fixed value of ω . For the first time, SLAC measured $\nu W_{2p}^{\text{EM}}(\nu, Q^2)$ vs. Q^2 at a fixed ω and found that the predictions of the parton model are correct, that is, the structure functions do scale. This can be seen from Figure 13.7.

The phenomenon of scaling observed in the SLAC experiment was explained in a simple model proposed by Feynman called the parton model which explains successfully many processes induced by electrons, muons, and neutrinos on nucleon and nuclear targets studied in the DIS region. The basic assumptions of this model are as follows:

- i) A rapidly moving hadron appears as a jet of partons, all of which travel more or less in the same direction as that of the parent hadron (Figure 13.8).

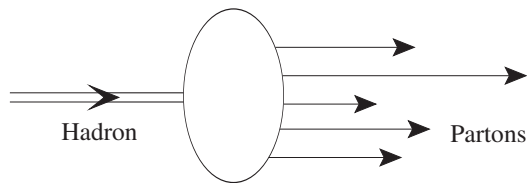


Figure 13.8 A rapidly moving hadron.

- ii) The basic process with free partons is calculated and then summed incoherently over the contributions of partons in the hadron (represented by the illustration on the left of Figure 13.9).

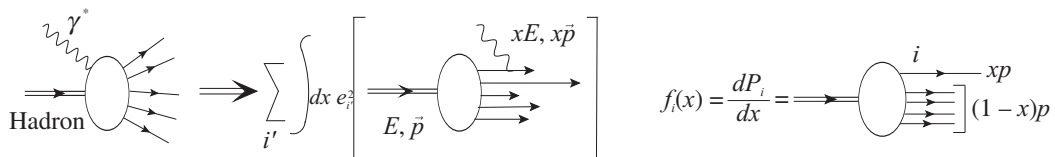


Figure 13.9 Figure on the left depicts the incoherent sum of the contributions and figure on the right represents momentum shared by the charged partons.

- iii) The three-momentum of the hadron is shared among the partons and one defines the parton momentum distribution (represented on the right side of Figure 13.9) as $f_i(x) = \frac{dP_i}{dx}$, where $f_i(x)$ is the probability that the struck charged parton i carries a fraction x of the hadron's four-momentum p .
- iv) These partons carry a fraction x of the hadron's momentum and energy (Table 13.1). All the fractions x add up to 1 such that

$$\sum_{i'} \int dx x f_{i'}(x) = 1,$$

where i' is the sum over the charged (quarks) as well as the neutral (gluons) partons.

Table 13.1 Kinematical quantities for hadron and parton.

Kinematic quantities	Hadron	Parton
Energy	E	xE
Momentum (longitudinal)	p_L	xp_L
Momentum (transverse)	$p_T = 0$	$xp_T = 0$
Mass	M	$m = xM$

The dimensionless structure functions for a parton struck by a charged lepton carrying a momentum fraction x and unit charge are given using Eqs. (13.23) and (13.24) as:

$$F_1(\omega) = \frac{Q^2}{4mvx} \delta\left(1 - \frac{Q^2}{2mv}\right), \quad F_2(\omega) = \delta\left(1 - \frac{Q^2}{2mv}\right),$$

where x is the fraction of momentum of the parton and $m = xM$. The structure functions for a proton F_{1p} and F_{2p} are written by summing the aforementioned expressions over all the partons that make up a proton (Figure 13.9), that is,

$$F_{2p}(\omega) = \sum_i \int dx e_i^2 f_i(x) x \delta\left(x - \frac{1}{\omega}\right),$$

$$F_{1p}(\omega) = \frac{\omega}{2} F_{2p}(\omega),$$

leading to

$$\nu W_{2p}(\nu, Q^2) \longrightarrow F_{2p}(x) = \sum_i e_i^2 x f_i(x), \quad (13.26)$$

$$MW_{1p}(\nu, Q^2) \longrightarrow F_{1p}(x) = \frac{1}{2x} F_{2p}(x), \quad (13.27)$$

where i corresponds to the charged partons (quarks). $F_{1p,2p}(x)$ correspond to the sum of the momentum fraction carried by all the quarks and antiquarks in the proton, weighted by the squares of the quark charges. Equation (13.27) leads to $F_{2p}(x) = 2xF_{1p}(x)$ which is known as the Callan–Gross relation (CGR) and is true when quarks are spin $\frac{1}{2}$ point objects.

Generally, the calculations for getting the proton ($F_{1,2}^p(x)$) or the neutron ($F_{1,2}^n(x)$) structure functions are performed in the four-flavor scheme assuming that heavy flavors (bottom and top) do not contribute as they are very massive in comparison to the nucleon's mass ($M \ll m_b$ or m_t). In the four-flavor scheme (considering only u , d , c , and s quarks), the proton structure function may be written in terms of the parton distribution functions as:

$$F_2^{ep}(x) = x \left[\frac{4}{9} (u(x) + \bar{u}(x) + c(x) + \bar{c}(x)) + \frac{1}{9} (d(x) + \bar{d}(x) + s(x) + \bar{s}(x)) \right]. \quad (13.28)$$

Similarly, in the case of the $e^- - n$ scattering process, where the role of up and down quarks are interchanged, one may write the structure function as:

$$F_2^{en}(x) = x \left[\frac{4}{9} (d(x) + \bar{d}(x) + c(x) + \bar{c}(x)) + \frac{1}{9} (u(x) + \bar{u}(x) + s(x) + \bar{s}(x)) \right]. \quad (13.29)$$

In these expressions, $u(x)$ is the probability distribution of the u quark in the proton or the d quark in the neutron ($u^p(x) = d^n(x) = u(x)$); similarly, $d(x)$ is the probability distribution of the d quark in the proton or the u quark in the neutron ($d^p(x) = u^n(x) = d(x)$), while the momentum distributions carried over by all the other flavors of quarks and antiquarks are taken to be the same as in the proton and neutron. $xu(x)$ represents the probability of finding an up quark with the target nucleon's momentum fraction x and so on. These probabilities are also known as parton distribution functions (PDFs). For an isoscalar nucleon target, the structure function is given by:

$$F_2^{eN}(x) = \frac{F_2^{ep}(x) + F_2^{en}(x)}{2}. \quad (13.30)$$

As partons carry the momentum fraction x of the target hadron's momentum, summing over the momentum of all the partons (charged as well as neutral ones) should result in 1, that is,

$$\int_0^1 dx \, x (u(x) + d(x) + s(x) + \bar{u}(x) + \bar{d}(x) + \bar{s}(x)) + \int_0^1 dx \, x g(x) = 1. \quad (13.31)$$

Experimentally, it was found that

$$\int_0^1 dx \, x (u(x) + d(x) + s(x) + \bar{u}(x) + \bar{d}(x) + \bar{s}(x)) \simeq 0.54. \quad (13.32)$$

Using this in Eq. (13.31) gives

$$\int_0^1 dx \, x g(x) \simeq 0.46. \quad (13.33)$$

Thus, approximately 50% of the hadron's momentum is carried by gluons. In the 'naive' parton model, one assumes that there are valence quarks (hereafter represented with a suffix v) and sea quarks (hereafter represented with a suffix s). The valence quarks contribute to the quantum numbers of hadron, while the sea quarks arise from the quark-antiquark pairs and gluons. In turn, the annihilation of the quark-antiquark pairs also gives rise to gluons. For example, in the case of proton, in the four-flavor scheme (u, d, c , and s), the probability distribution of various quarks in proton are:

$$\begin{aligned} u(x) &= u_v(x) + u_s(x); \quad d(x) = d_v(x) + d_s(x); \quad u_v(x) = 2d_v(x), \\ s_v(x) &= \bar{u}_v(x) = \bar{d}_v(x) = \bar{s}_v(x) = c_v(x) = \bar{c}_v(x) = 0, \\ u_s(x) &= \bar{u}_s(x) = d_s(x) = \bar{d}_s(x) = s_s(x) = \bar{s}_s(x) = c_s(x) = \bar{c}_s(x) \equiv S(x). \end{aligned} \quad (13.34)$$

For the nucleon structure functions, various parameterizations of parton density distribution functions are available in the literature such as GRV [549], MSTW [550], CTEQ6.6 [551], MMHT [552], etc. The dependence of the parton probability densities on the Bjorken scaling variable is shown in Figure 13.10 in the range of $2 \leq Q^2 \leq 10 \text{ GeV}^2$. From the figure, one can see that valence quarks dominate in the region of mid and high x while sea quarks dominate

in the low x region. Moreover, with increase in Q^2 , the contribution of valence quarks get reduced, whereas the contribution of sea quarks get enhanced.

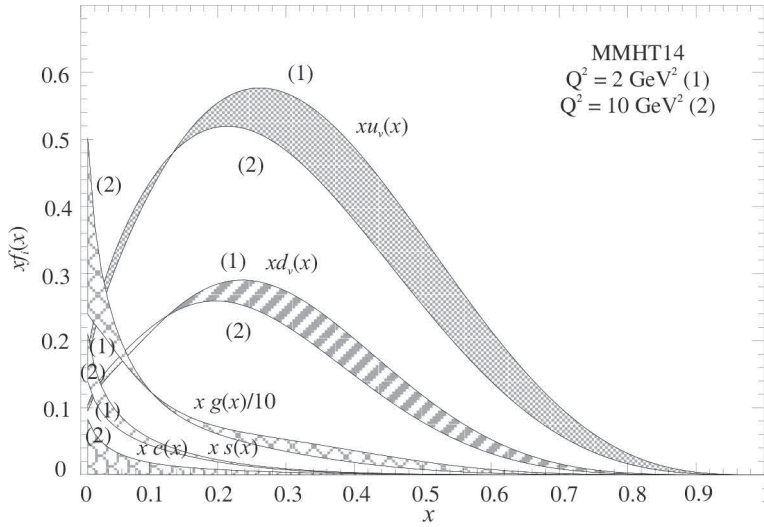


Figure 13.10 Parton density distribution functions using MMHT PDFs parameterization [552] at leading order for $2 \text{ GeV}^2 \leq Q^2 \leq 10 \text{ GeV}^2$.

The contribution of valence and sea quarks in the structure functions can be understood by taking the ratio of $\frac{F_2^{en}(x)}{F_2^{ep}(x)}$ and using Eq. (13.34) which results in:

$$\begin{aligned} \frac{F_2^{en}(x)}{F_2^{ep}(x)} &= \frac{x \left[\frac{1}{9} (u_v(x) + 2S(x)) + \frac{4}{9} (d_v(x) + 2S(x)) + \frac{1}{9} (2S(x)) + \frac{4}{9} (2S(x)) \right]}{x \left[\frac{4}{9} (u_v(x) + 2S(x)) + \frac{1}{9} (d_v(x) + 2S(x)) + \frac{1}{9} (2S(x)) + \frac{4}{9} (2S(x)) \right]}, \\ &= \frac{\left[\frac{1}{9} u_v(x) + \frac{4}{9} d_v(x) + \frac{1}{9} (20S(x)) \right]}{\left[\frac{4}{9} u_v(x) + \frac{1}{9} d_v(x) + \frac{1}{9} (20S(x)) \right]} \end{aligned}$$

which simplifies to

$$\frac{F_2^{en}(x)}{F_2^{ep}(x)} = \begin{cases} \frac{[u_v(x) + 4d_v(x)]}{[4u_v(x) + d_v(x)]} & \text{if valence quarks dominate} \\ \frac{1}{4} & \text{if valence } u \text{ quark dominates} \\ 4 & \text{if valence } d \text{ quark dominates} \\ 1 & \text{if sea-quarks dominate.} \end{cases}$$

The ratio $\frac{F_2^{en}(x)}{F_2^{ep}(x)}$ has been experimentally measured in different experiments for a wide range of x . The experimental observations are presented in Figure 13.11, from which it can be inferred that the valence u quarks in the protons (and d quarks in the neutrons) dominate at large x ; the

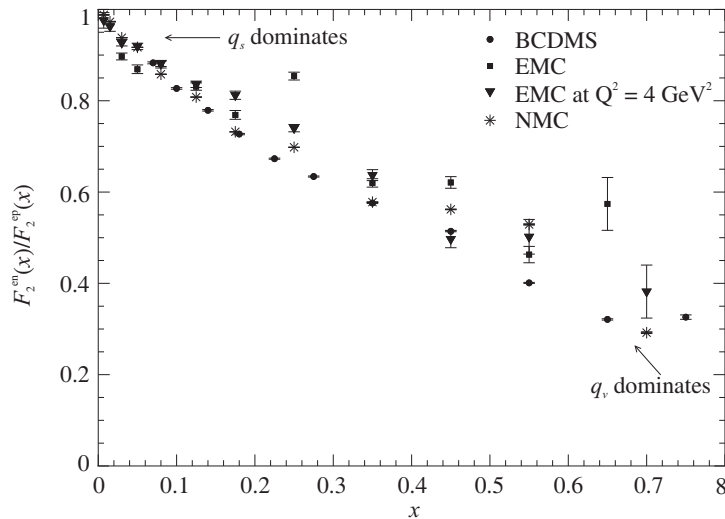


Figure 13.11 Experimental measurements for $\frac{F_2^{en}(x)}{F_2^{ep}(x)}$ vs. x [553, 554, 555, 556] for proton and neutron targets in the case of electromagnetic interaction.

sea quarks dominate at small x . However, valence d quarks (u quarks) never dominate in the case of proton (neutron). If one plots the difference of the electromagnetic structure functions in neutrons ($F_2^{en}(x)$) and protons ($F_2^{ep}(x)$) by using Eqs. (13.28), (13.29), and (13.34), that is,

$$F_2^{ep}(x) - F_2^{en}(x) = \frac{1}{3}x[u_v(x) - d_v(x)], \quad (13.35)$$

then the peak should occur at $x = 1/3$ (two valence u quarks and one valence d quark in the

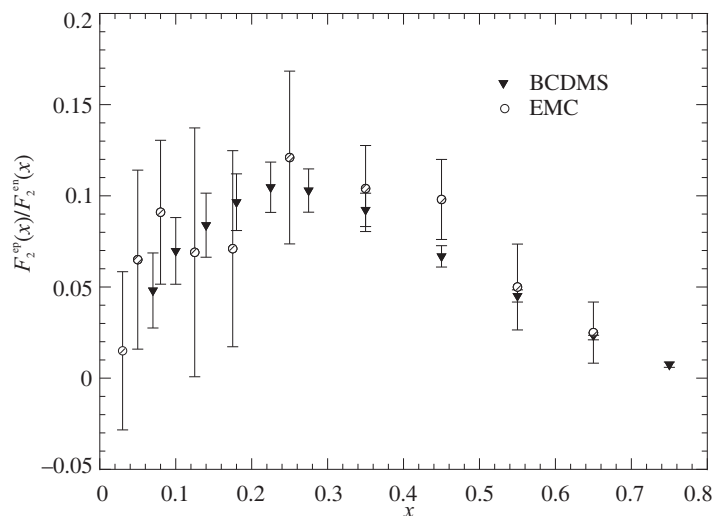


Figure 13.12 Experimental measurements for $F_2^{ep}(x) - F_2^{en}(x)$ vs. x [553, 554] for proton and neutron targets in the case of electromagnetic interaction.

proton and vice versa for the neutron). This indeed has been observed and it is shown here in Figure 13.12.

At low Q^2 , the nucleon structure functions were experimentally found to be x as well as Q^2 dependent [548, 557, 558, 559, 560, 561, 562]; this was also suggested by the perturbative QCD. It is important to point out that if one incorporates the gluon emission, then Bjorken scaling gets violated. Scaling violation will be discussed in some detail in Section 13.5. In the next section, we present the argument in support of spin 1/2 nature of charged partons.

Photoabsorption cross section, Callan–Gross relation, and spin 1/2 nature of quarks

The electron scattering cross section is considered to be the sum of the longitudinal and transverse polarized virtual photon scattering cross sections. The total scattering cross section for the interaction of a virtual polarized photon with an unpolarized nucleon target is given by [238]:

$$\sigma^\lambda = \frac{4\pi^2\alpha}{K} \epsilon_\mu^\lambda \epsilon_\nu^{\lambda*} W_N^{\mu\nu}, \quad (13.36)$$

where ϵ_μ^λ is the photon polarization vector such that ϵ_μ^0 describes the longitudinally polarized virtual photons for zero helicity state, that is, $\lambda = 0$, while $\epsilon^{(+1)}$ and $\epsilon^{(-1)}$ describe the transversely polarized states with helicity $\lambda = +1$ and $\lambda = -1$, respectively, corresponding to right- and left-handed virtual photons. Let us assume that the photon is traversing along the Z -axis with $q^\mu = (\sqrt{Q^2 + \nu^2}, 0, 0, \nu)$; then, the corresponding polarization states are given by:

$$\epsilon_{\lambda=0}^\mu = \frac{1}{\sqrt{Q^2}} (\sqrt{Q^2 + \nu^2}, 0, 0, \nu), \quad (13.37)$$

$$\epsilon_{\lambda=+1}^\mu = -\frac{1}{\sqrt{2}} (0, 1, +i, 0), \quad (13.38)$$

$$\epsilon_{\lambda=-1}^\mu = +\frac{1}{\sqrt{2}} (0, 1, -i, 0). \quad (13.39)$$

The Lorenz gauge invariance demands that $\partial_\mu A^\mu = 0$ with $A^\mu = \epsilon^\mu e^{-iq \cdot x}$ which leads to $q \cdot \epsilon = 0$. This implies that the components of polarization vectors are orthogonal to the momentum transfer q such that $\epsilon_{(+1)} \cdot q = \epsilon_{(-1)} \cdot q = \epsilon_{(0)} \cdot q = 0$ and obey the orthogonality relation $\epsilon_{(\pm 1)} \cdot \epsilon_{(0)} = 0$. The factor K in Eq. (13.36) is defined as the energy required to create the final hadronic state X and is given by:

$$K = \frac{W^2 - M^2}{2M},$$

with W^2 as the square of the invariant mass of the final hadronic state. The nucleon structure functions $F_{1N}^{\text{EM}}(x, Q^2)$ and $F_{2N}^{\text{EM}}(x, Q^2)$ are related to the transverse (σ_T) and longitudinal (σ_L)

photo absorption scattering cross sections and are given by using Eqs. (13.7) and (13.36) as [238]:

$$\sigma_T^{\text{EM}}(x, Q^2) = \frac{\sigma(\lambda = +1) + \sigma(\lambda = -1)}{2} = \frac{4\pi^2\alpha}{KM} F_{1N}^{\text{EM}}(x, Q^2) \quad (13.40)$$

$$\begin{aligned} \sigma_L^{\text{EM}}(x, Q^2) &= \sigma(\lambda = 0) = \frac{4\pi^2\alpha}{KM} \left[\left(1 + \frac{\nu^2}{Q^2}\right) \frac{M}{\nu} F_{2N}^{\text{EM}}(x, Q^2) \right. \\ &\quad \left. - F_{1N}^{\text{EM}}(x, Q^2) \right]. \end{aligned} \quad (13.41)$$

It is important to point out that in the case of electromagnetic interaction, where parity is conserved, $\sigma(\lambda = +1) = \sigma(\lambda = -1)$. Hence, the differential scattering cross section given in Eq. (13.18) may be recast as

$$\frac{d^2\sigma_N^{\text{EM}}}{d\Omega'_l dE'_l} = \left(\frac{\alpha E'_l}{4\pi^2 Q^2 M E_l (1 - \epsilon)} \right) \sigma_T^{\text{EM}}(x, Q^2) \left[1 + \epsilon R_L^{\text{EM}}(x, Q^2) \right], \quad (13.42)$$

where

$$R_L^{\text{EM}}(x, Q^2) = \frac{\sigma_L^{\text{EM}}(x, Q^2)}{\sigma_T^{\text{EM}}(x, Q^2)} \quad (13.43)$$

and

$$\epsilon = \left[1 + 2 \left(1 + \frac{\nu^2}{Q^2} \right) \tan^2 \frac{\theta}{2} \right]^{-1} = \frac{1 - y - \frac{M^2 x^2 y^2}{Q^2}}{1 - y + \frac{y^2}{2} + \frac{M^2 x^2 y^2}{Q^2}}, \quad \text{with } y = \frac{\nu}{E}. \quad (13.44)$$

This expression for $R_L^{\text{EM}}(x, Q^2)$ defines the ratio of the probability of longitudinally polarized to transversely polarized photon absorption cross sections. It may be noticed from Eqs. (13.42) and (13.44) that for $y \rightarrow 0$, the value of ϵ will be large; therefore, the contribution to the differential scattering cross section from the longitudinal part (σ_L) will be maximum. However, for $y \rightarrow 1$, ϵ approaches zero and the transverse part (σ_T) will give the maximum contribution to the scattering cross section.

Moreover, by using Eqs. (13.40) and (13.41), one may write the nucleon structure functions $F_{1N}^{\text{EM}}(x, Q^2)$ and $F_{2N}^{\text{EM}}(x, Q^2)$ in terms of $\sigma_T^{\text{EM}}(x, Q^2)$ and $\sigma_L^{\text{EM}}(x, Q^2)$ as

$$\begin{aligned} F_{1N}^{\text{EM}}(x, Q^2) &= \frac{KM}{4\pi^2\alpha} \sigma_T^{\text{EM}}(x, Q^2), \\ F_{2N}^{\text{EM}}(x, Q^2) &= \frac{K\nu}{4\pi^2\alpha} \left(1 + \frac{\nu^2}{Q^2} \right)^{-1} [\sigma_L^{\text{EM}}(x, Q^2) + \sigma_T^{\text{EM}}(x, Q^2)]. \end{aligned} \quad (13.45)$$

It may be noticed that $F_{1N}^{\text{EM}}(x, Q^2)$ has contribution only from transversely polarized photons while the contribution to $F_{2N}^{\text{EM}}(x, Q^2)$ comes from both the longitudinally as well as the

transversely polarized photons. Therefore, in order to obtain the contribution from the longitudinal part only, the longitudinal structure function $F_{LN}^{\text{EM}}(x, Q^2)$ is defined as:

$$F_{LN}^{\text{EM}}(x, Q^2) = \frac{2x\nu(1-x)M}{4\pi^2\alpha}\sigma_L^{\text{EM}}(x, Q^2) = \gamma^2 F_{2N}^{\text{EM}}(x, Q^2) - 2xF_{1N}^{\text{EM}}(x, Q^2), \quad (13.46)$$

$$\text{where } \gamma^2 = \left(1 + \frac{4M^2x^2}{Q^2}\right).$$

To illustrate this further, let us discuss the ratio $R_L^{\text{EM}}(x)$ for a nucleon target defined in Eq. (13.43) by redefining $R_L^{\text{EM}}(x, Q^2)$ in terms of structure functions, that is,

$$\begin{aligned} R_L^{\text{EM}}(x, Q^2) &= \frac{\sigma_L^{\text{EM}}(x, Q^2)}{\sigma_T^{\text{EM}}(x, Q^2)} = \frac{F_{LN}^{\text{EM}}(x, Q^2)}{2xF_{1N}^{\text{EM}}(x, Q^2)} \\ &= \left(1 + \frac{4M^2x^2}{Q^2}\right) \frac{F_{2N}^{\text{EM}}(x, Q^2)}{2xF_{1N}^{\text{EM}}(x, Q^2)} - 1. \end{aligned} \quad (13.47)$$

The ratio $\frac{2xF_{1p}^{\text{EM}}(x)}{F_{2p}^{\text{EM}}(x)}$ has been measured at SLAC [563] and found to be $\frac{2xF_{1p}^{\text{EM}}(x)}{F_{2p}^{\text{EM}}(x)} \approx 1$ (Figure 13.13: left panel). It also verifies the Callan–Gross relation (Eq.13.27). Using CGR in Eq. (13.47), we may write:

$$R_L^{\text{EM}}(x, Q^2) = \frac{\sigma_L^{\text{EM}}(x, Q^2)}{\sigma_T^{\text{EM}}(x, Q^2)} = \frac{4M^2x^2}{Q^2}, \quad (13.48)$$

which is referred to as the ‘CGR limit’; it tends to zero as Q^2 goes to infinity, that is,

$$R_L^{\text{EM}}(x, Q^2) \rightarrow 0 \text{ as } Q^2 \rightarrow \infty. \quad (13.49)$$

This is evidence for the spin 1/2 nature of quarks (Figure 13.13: right panel).

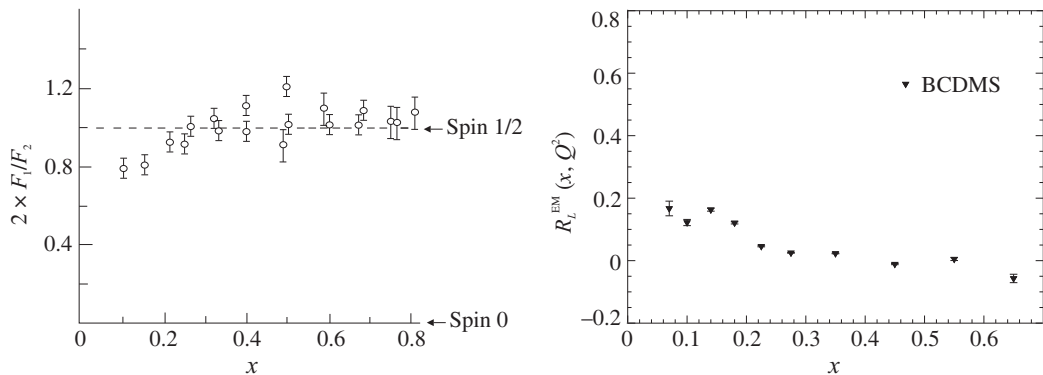


Figure 13.13 Left panel: Experimental verification of the Callan–Gross relation for the spin 1/2 nature of quarks [563]. Right panel: Experimental results for the ratio of $R_L^{\text{EM}}(x, Q^2) = \frac{F_L^{\text{EM}}(x, Q^2)}{2xF_1^{\text{EM}}(x, Q^2)}$ [557].

Furthermore, to understand the spin 1/2 nature of charged partons, let us recall the elastic electron scattering with spin 1/2 (Eq. (9.16) and Eq. (10.55)) as well as with spin zero particles (Eq. (10.24)). Notice that for the spin 1/2 particles, the expression of differential cross section have terms both with $\sin^2 \theta$ and $\cos^2 \theta$ (as shown for $e^- - p$ DIS in Eq. (13.25)), while for the spin 0 particle, terms with only $\cos^2 \theta$ contribute (Eq. (10.24)). Suppose that quarks have zero spin; then by comparing Eq. (13.25) with Eq. (10.24), it may be observed that the transverse structure function $F_{1N}^{\text{EM}}(x) \rightarrow 0$, which leads to $\sigma_T^{\text{EM}}(x, Q^2) \rightarrow 0$, implying that $R_L^{\text{EM}}(x, Q^2) \rightarrow \infty$. While, for the spin 1/2 quarks, both the structure functions $F_{1N}^{\text{EM}}(x)$ and $F_{2N}^{\text{EM}}(x)$ contribute which are related by the Callan–Gross relation (Figure 13.13).

This behavior can also be understood by looking at Figure 13.14, where the collision of a quark (constituent of proton) with an intermediate virtual photon is shown in the Breit frame. If one choose the Z-axis along the three momentum \vec{p} , then from the conservation of

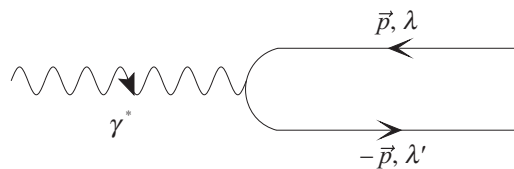


Figure 13.14 Head on collision of a quark with a virtual photon. λ and λ' denote the initial and final helicity states.

angular momentum (J_Z), a spin 0 quark cannot absorb a transverse photon as it has left- and right-handed helicity states ($\lambda = \pm 1$) which results in

$$\sigma_T^{\text{EM}} \rightarrow 0 \quad \Rightarrow \quad R_L^{\text{EM}} = \frac{\sigma_L^{\text{EM}}}{\sigma_T^{\text{EM}}} \rightarrow \infty.$$

For a spin half quark whose helicity is conserved in a high energy interaction process, the possible interaction is only with the transverse photons with left- and right-handed helicities. Therefore, the contribution from the longitudinal photons will be zero,

$$\sigma_L^{\text{EM}} \rightarrow 0, \quad \Rightarrow \quad R_L^{\text{EM}} = \frac{\sigma_L^{\text{EM}}}{\sigma_T^{\text{EM}}} \rightarrow 0.$$

In the electron scattering experiments at BCDMS [557], a very small but finite (close to zero) value of the ratio $R_L^{\text{EM}}(x, Q^2)$ was measured (Figure 13.13), which is an evidence of the spin 1/2 nature of partons.

13.2.2 Differential scattering cross section in terms of dimensionless variables x and y

The differential scattering cross section $\frac{d^2\sigma}{d\Omega' dE'}$ given in Eq. (13.25) may be expressed in terms of the dimensionless variables, known as the Bjorken variable x and inelasticity $y \left(= \frac{p \cdot q}{p \cdot k} = \frac{\nu}{E_l} \right)$, using the relationship:

$$\frac{\pi}{E_l E_l'} dQ^2 d\nu = d\Omega_l' dE_l' = \frac{2ME_l}{E_l'} \pi y dx dy, \quad (13.50)$$

resulting in

$$\frac{d^2\sigma}{dx dy} = \frac{8\pi\alpha^2 ME_l}{Q^4} \left[F_{2N}^{\text{EM}}(x) \left(1 - y - \frac{Mxy}{2E_l} \right) + xy^2 F_{1N}^{\text{EM}}(x) \right]. \quad (13.51)$$

For the study of the nucleon structure, a complete knowledge of the structure functions over the entire range of the scaling variables is required, which for a non-zero leptonic mass, lies in the following kinematical range

$$\frac{m_l^2}{2M(E_l - m_l)} \leq x \leq 1 \quad (13.52)$$

$$(y_1 - y_2) \leq y \leq (y_1 + y_2), \quad (13.53)$$

where

$$y_1 = \frac{1 - m_l^2 \sqrt{\left(\frac{1}{2ME_l x} + \frac{1}{2E_l^2} \right)}}{2 \left(1 + \frac{Mx}{2E_l} \right)} \quad \text{and} \quad y_2 = \frac{\sqrt{\left(1 - \frac{m_l^2}{2ME_l x} \right)^2 - \frac{m_l^2}{E_l^2}}}{2 \left(1 + \frac{Mx}{2E_l} \right)}. \quad (13.54)$$

In the massless lepton limit, this will reduce to $0 \leq x \leq 1$ and $0 \leq y \leq \frac{1}{1 + \frac{Mx}{2E_l}}$. In Figure 13.15, the allowed kinematic regions for elastic, inelastic, and deep inelastic scattering processes are shown in the $Q^2 - \nu$ plane. The line of $W = M$ corresponds to the kinematical limit of elastic scattering, where $Q^2 = 2M\nu$, that is, $x = 1$. To separate the kinematical region in the (Q^2, ν)

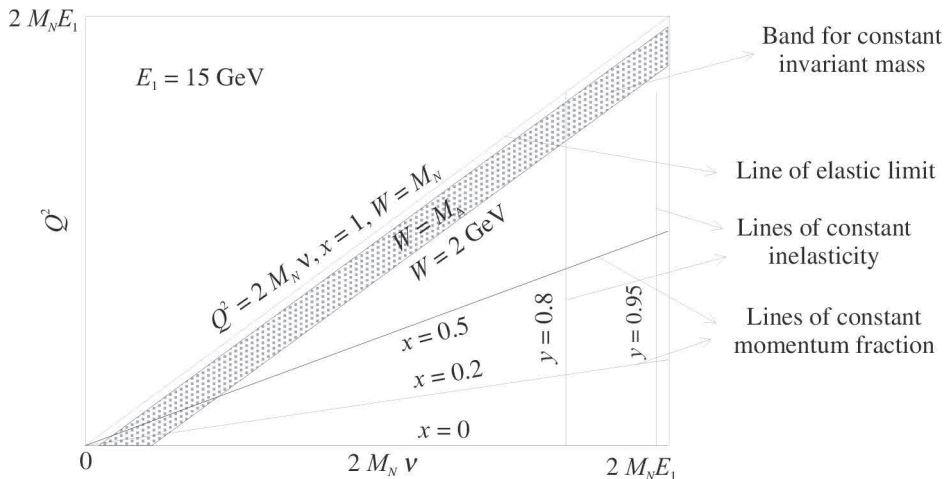


Figure 13.15 Variation of kinematic variables such as x , y , and W is shown in the $Q^2 - \nu$ plane.

plane from the resonance region, a band is shown for the constant values of invariant mass W separate from the mass of lowest lying resonance ($P_{33}(1232)$), that is, $W = M_\Delta$ to $W = 2 \text{ GeV}$. It is noticeable that the lines of constant invariant mass are parallel to the line of elastic limit, that is, $W = M$ and $x = 1$. The kinematical region of DIS, corresponding to the different values of the Bjorken variable x such as 0.5, 0.2, and 0, is shown, for which the corresponding lines lie below the resonance band except for some overlapped part in the low ν region.

DIS cross section (Eq. (13.51)) may also be written in terms of the Mandelstam variables s , t , and u ,

$$\begin{aligned} s &= (k + p)^2 = (k' + p')^2 \simeq 2p \cdot k \text{ or } 2p' \cdot k', \\ t &= (k - k')^2 = (p' - p)^2 \simeq -2k \cdot k' \text{ or } -2p \cdot p', \\ u &= (p - k')^2 = (p' - k)^2 \simeq -2p \cdot k' \text{ or } -2p' \cdot k, \text{ and using them we may write} \\ x &= \frac{Q^2}{2M\nu} = -\frac{t}{s+u} \text{ and } y = \frac{s+u}{s}, \end{aligned} \quad (13.55)$$

resulting in

$$\frac{d^2\sigma^{\text{EM}}}{dtdu} = \frac{4\pi\alpha^2}{2t^2s^2(s+u)} \left\{ 2xF_{1N}^{\text{EM}}(x)(s+u)^2 - 2usF_{2N}^{\text{EM}}(x) \right\}. \quad (13.56)$$

13.3 Deep Inelastic Charged Current $\nu_l/\bar{\nu}_l - N$ Scattering

The charged current deep inelastic scattering for the weak interaction process (shown in Figure 13.16)

$$\nu_l/\bar{\nu}_l(k) + N(p) \rightarrow l^-/l^+(k') + X(p'); \quad l = e, \mu \quad (13.57)$$

takes place via the exchange of vector bosons (W^+/W^-) when (anti)neutrino beam interact with a target nucleon (N) and gives rise to a jet of hadrons (X) in the final state. For the reaction in Eq. (13.57), the quantities within the parenthesis correspond to the four-momenta of the respective particle.

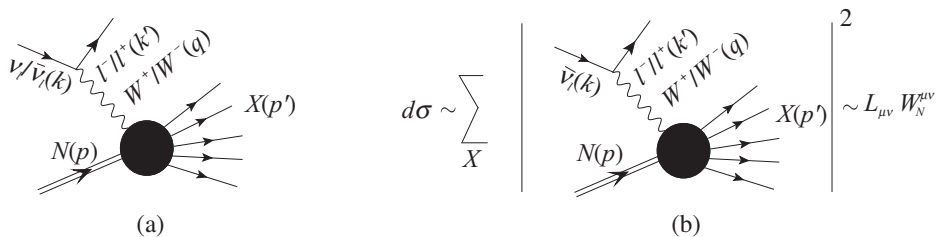


Figure 13.16 (a) Feynman diagram for the (anti)neutrino induced deep inelastic scattering process, (b) Summation over the final hadronic state X and its amplitude square corresponds to the scattering cross section.

The $V - A$ interaction allows only neutrinos with negative (left-handed) helicity and antineutrinos with positive (right-handed) helicity to participate in the process. The leptonic and hadronic vertices are shown in Figure 13.17, where the strength of the weak interaction, $\frac{-ig_W}{2\sqrt{2}}$ at the vertices is related to G_F (Chapter 8). For an inclusive $\nu_l/\bar{\nu}_l$ induced DIS process on a free nucleon target in the laboratory frame (Figure 13.16), the double differential scattering cross section is expressed as

$$\frac{d^2\sigma_N^{WI}}{d\Omega'_l dE'_l} = \frac{1}{2\pi^2} \frac{|\vec{k}'|}{|\vec{k}|} \overline{\sum} \sum |\mathcal{M}|^2, \quad (13.58)$$

where the amplitude square is given by

$$\overline{\sum} \sum |\mathcal{M}|^2 = \frac{G_F^2}{2} \left(\frac{M_W^2}{Q^2 + M_W^2} \right)^2 L_{\mu\nu}^{WI} W_N^{\mu\nu}. \quad (13.59)$$

$L_{\mu\nu}^{WI}$ is the leptonic tensor and is expressed as

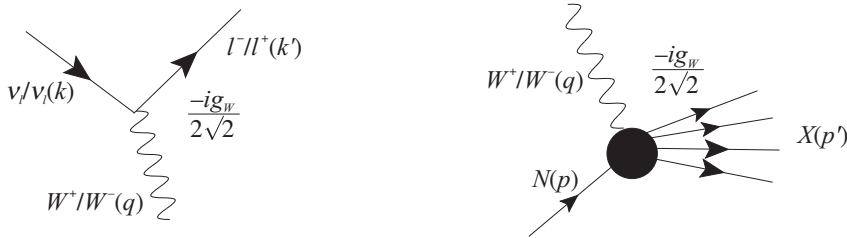


Figure 13.17 Feynman representation for leptonic and hadronic vertices (left and right columns) in the case of weak interaction. Feynman diagram showing the $\nu - N$ scattering for the summed over hadronic states X .

$$L_{\mu\nu}^{WI} = \underbrace{8(k_\mu k'_\nu + k_\nu k'_\mu - k \cdot k' g_{\mu\nu})}_{\text{symmetric}} \pm \underbrace{i\epsilon_{\mu\nu\rho\sigma} k^\rho k'^\sigma}_{\text{antisymmetric}}, \quad (13.60)$$

It has an antisymmetric term due to the axial vector part with a +ve sign for antineutrinos and a -ve sign for neutrinos. $W_N^{\mu\nu}$ is the hadronic tensor which in general is written in terms of the weak structure functions $W_{iN}^{WI}(\nu, Q^2)$ ($i = 1 - 6$) as

$$\begin{aligned} W_N^{\mu\nu} = & \left(\frac{q^\mu q^\nu}{q^2} - g^{\mu\nu} \right) W_{1N}^{WI}(\nu, Q^2) + \frac{W_{2N}^{WI}(\nu, Q^2)}{M^2} \left(p^\mu - \frac{p \cdot q}{q^2} q^\mu \right) \left(p^\nu - \frac{p \cdot q}{q^2} q^\nu \right) \\ & - \frac{i}{2M^2} \epsilon^{\mu\nu\rho\sigma} p_\rho q_\sigma W_{3N}^{WI}(\nu, Q^2) + \frac{W_{4N}^{WI}(\nu, Q^2)}{M^2} q^\mu q^\nu \\ & + \frac{W_{5N}^{WI}(\nu, Q^2)}{M^2} (p^\mu q^\nu + q^\mu p^\nu) + \frac{i}{M^2} (p^\mu q^\nu - q^\mu p^\nu) W_{6N}^{WI}(\nu, Q^2). \end{aligned} \quad (13.61)$$

In the limit of massless lepton ($m_l \rightarrow 0$), the terms depending on $W_{4N}^{WI}(\nu, Q^2)$, $W_{5N}^{WI}(\nu, Q^2)$, and $W_{6N}^{WI}(\nu, Q^2)$ will not contribute to the scattering cross section. The additional structure function $W_{3N}^{WI}(\nu, Q^2)$ arises due to parity violation in weak interactions. Therefore, it carries opposite signs for neutrinos and antineutrinos. $W_N^{\mu\nu}$ in the limit of $m_l \rightarrow 0$ are then given by:

$$\begin{aligned} W_N^{\mu\nu} = & \left(\frac{q^\mu q^\nu}{q^2} - g^{\mu\nu} \right) W_{1N}^{WI}(\nu, Q^2) + \frac{W_{2N}^{WI}(\nu, Q^2)}{M^2} \left(p^\mu - \frac{p \cdot q}{q^2} q^\mu \right) \left(p^\nu - \frac{p \cdot q}{q^2} q^\nu \right) \\ & - \frac{i}{2M^2} \epsilon^{\mu\nu\rho'\sigma'} p_{\rho'} q_{\sigma'} W_{3N}^{WI}(\nu, Q^2). \end{aligned} \quad (13.62)$$

Using Eqs. (13.59), (13.60), and (13.62), the differential scattering cross section given in Eq. (13.58) simplifies to

$$\begin{aligned} \frac{d^2\sigma_N^{WI}}{d\Omega'dE'} &= \frac{G_F^2 E_l'^2 \cos^2\left(\frac{\theta}{2}\right)}{2\pi^2} \left(\frac{M_W^2}{M_W^2 + Q^2}\right)^2 \left[2 \tan^2\left(\frac{\theta}{2}\right) W_{1N}^{WI}(x, Q^2) \right. \\ &\quad \left. + W_{2N}^{WI}(x, Q^2) \pm \left(\frac{E_l + E_l'}{M}\right) \tan^2\left(\frac{\theta}{2}\right) W_{3N}^{WI}(x, Q^2) \right]. \end{aligned} \quad (13.63)$$

Following the same analogy as discussed in Section 13.2, the weak nucleon structure functions $W_{iN}^{WI}(\nu, Q^2)$ ($i = 1, 2, 3$) are written in terms of the dimensionless nucleon structure functions $F_{iN}^{WI}(x, Q^2)$ ($i = 1, 2, 3$) as:

$$\left. \begin{aligned} MW_{1N}^{WI}(\nu, Q^2) &= F_{1N}^{WI}(x, Q^2), \\ \nu W_{2N}^{WI}(\nu, Q^2) &= F_{2N}^{WI}(x, Q^2), \\ \nu W_{3N}^{WI}(\nu, Q^2) &= F_{3N}^{WI}(x, Q^2). \end{aligned} \right\} \quad (13.64)$$

Using Eqs. (13.64), the differential scattering cross section is then written as:

$$\begin{aligned} \frac{d^2\sigma_N^{WI}}{d\Omega'_l dE'_l} &= \frac{G_F^2 E_l'^2 \cos^2\left(\frac{\theta}{2}\right)}{2\pi^2 M \nu} \left(\frac{M_W^2}{M_W^2 + Q^2}\right)^2 \left[2\nu \tan^2\left(\frac{\theta}{2}\right) F_{1N}^{WI}(x, Q^2) \right. \\ &\quad \left. + M F_{2N}^{WI}(x, Q^2) \pm (E_l + E_l') \tan^2\left(\frac{\theta}{2}\right) F_{3N}^{WI}(x, Q^2) \right], \end{aligned} \quad (13.65)$$

where the term corresponding to $F_{3N}^{WI}(x, Q^2)$ will have a positive sign for neutrinos and a negative sign for antineutrinos. This scattering cross section can also be written in terms of the Bjorken scaling variables x and y as

$$\begin{aligned} \frac{d^2\sigma_N^{WI}}{dx dy} &= \frac{G_F^2 s}{2\pi} \left[xy^2 F_{1N}^{WI}(x, Q^2) + \left(1 - y - \frac{Mxy}{2E_l}\right) F_{2N}^{WI}(x, Q^2) \right. \\ &\quad \left. \pm xy \left(1 - \frac{y}{2}\right) F_{3N}^{WI}(x, Q^2) \right], \end{aligned} \quad (13.66)$$

where the propagator term $\left(\frac{M_W^2}{M_W^2 + Q^2}\right)^2 \approx 1$ for $M_W^2 \gg Q^2$. Since the virtual bosons may have longitudinal as well as transverse polarization states, the nucleon structure functions are also written in terms of the longitudinal and transverse absorption cross section as

$$\sigma_{(\lambda=\pm 1)}^{WI}(x, Q^2) = \frac{G\pi\sqrt{2}}{KM} \left(F_{1N}^{WI}(x, Q^2) \pm \frac{1}{2} \sqrt{1 + \frac{4M^2 x^2}{Q^2}} F_{3N}^{WI}(x, Q^2) \right), \quad (13.67)$$

$$\sigma_T^{WI}(x, Q^2) = \frac{\sigma_{(\lambda=+1)}^{WI}(x, Q^2) + \sigma_{(\lambda=-1)}^{WI}(x, Q^2)}{2}, \quad (13.68)$$

$$\sigma_{(\lambda=0)}^{WI}(x, Q^2) = \sigma_L^{WI}(x, Q^2) = \frac{G\pi\sqrt{2}}{2 x KM} F_{LN}^{WI}(x, Q^2), \quad (13.69)$$

where the longitudinal structure function for weak interactions is defined as

$$F_{LN}^{WI}(x, Q^2) = \left(1 + \frac{4M^2x^2}{Q^2}\right) F_{2N}^{WI}(x, Q^2) - 2xF_{1N}^{WI}(x, Q^2). \quad (13.70)$$

For weak interactions at low Q^2 , the transverse structure function ($F_{1N}^{WI}(x, Q^2)$) vanishes while the longitudinal structure function ($F_{LN}^{WI}(x, Q^2)$) dominates. This is due to the contribution from vector (V) as well as axial vector (A) components. For the transverse structure function, both axial vector and vector components vanish at low Q^2 . For the longitudinal structure function too, the vector component becomes zero by applying CVC but the axial vector component which is related to the PCAC, gives a non-zero contribution. Therefore, the ratio $R_L^{WI}(x, Q^2)$ diverges in the case of weak interaction induced processes, that is,

$$R_L^{WI}(x, Q^2) = \frac{F_{LN}^{WI}(x, Q^2)}{2xF_{1N}^{WI}(x, Q^2)} \text{ as } Q^2 \rightarrow 0 \quad \text{and} \quad \frac{F_{LN}^{WI,AV}(x, Q^2)}{0} \rightarrow \infty.$$

An important feature of weak interaction processes is that through $\nu_l/\bar{\nu}_l$ scattering on nucleons, quarks and antiquarks can be directly observed which is not possible in the case of electromagnetic interactions. For the charged current weak interaction processes, there are two possibilities:

- For a neutrino beam, the mediating quanta W^+ interacts with d , s , \bar{u} , and \bar{c} flavors on the proton target because of the charge conservation at the weak vertex (Figure 13.18 (top panel)).
- For an antineutrino beam, the mediating quanta W^- interacts with the u , c , \bar{d} , and \bar{s} flavors on the proton target due to the conservation of charge at the weak vertex (Fig.13.18 (bottom panel)).

In the case of a neutron target, the role of the u and d quarks are interchanged. In the parton model, the partons are free inside the nucleon, then the neutrino–quark (antineutrino–antiquark) interactions will be similar to the case of neutrino–electron (antineutrino–positron) interaction processes as discussed in Chapter 9. Recall the expression of the scattering cross section for neutrino–electron (antineutrino–positron) interaction processes (Chapter 9) in terms of the Mandelstam variables, which may be written as

$$\frac{d\sigma}{dy} = \frac{G_F^2 s}{\pi}; \quad s = (p+k)^2 \simeq 2p \cdot k. \quad (13.71)$$

Similarly, for the antineutrino–electron (neutrino–positron) interaction processes, the differential cross section is given by

$$\frac{d\sigma}{dy} = \frac{G_F^2 s}{\pi} (1-y)^2. \quad (13.72)$$

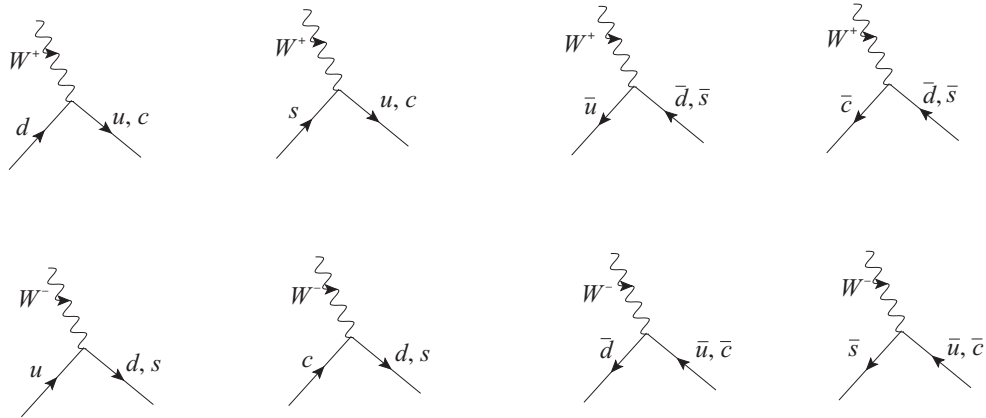


Figure 13.18 Feynman diagram for W^\pm interactions with quarks and antiquarks.

The expressions of scattering cross section for $\nu_l - q$ ($\bar{\nu}_l - \bar{q}$) and $\nu_l - \bar{q}$ ($\bar{\nu}_l - q$) interaction processes would be similar to the cross section of $\nu_l - e^-$ ($\bar{\nu}_l - e^+$) given in Eq. (13.71) and $\bar{\nu}_l - e^-$ ($\nu_l - e^+$) given in Eq. (13.72), respectively. The center of mass energy (W) for $\nu_l - q$ ($\bar{\nu}_l - \bar{q}$), and $\nu_l - \bar{q}$ ($\bar{\nu}_l - q$) scattering processes is

$$W = \sqrt{s'^2}, \text{ where } s' = (xp + k)^2 \simeq 2xp \cdot k = xs. \quad (13.73)$$

Here, x is the momentum fraction carried by each quark or antiquark of the parent nucleon's momentum. Therefore, similar to Eqs. (13.71) and (13.72), the scattering cross sections are obtained as

$$\frac{d\sigma^{\nu q/\bar{\nu}\bar{q}}}{dy} = \frac{G_F^2 s x}{\pi}, \quad \frac{d\sigma^{\nu\bar{q}/\bar{\nu}q}}{dy} = \frac{G_F^2 s x}{\pi} (1-y)^2. \quad (13.74)$$

These expressions are valid for the four flavors of quarks which are treated as massless. The integration over y in Eq. (13.74) between the limits 0 and 1 results in

$$\sigma^{\nu q/\bar{\nu}\bar{q}} = \frac{G_F^2 s x}{\pi}, \quad \sigma^{\nu\bar{q}/\bar{\nu}q} = \frac{G_F^2 s x}{3\pi} \Rightarrow \frac{\sigma^{\nu q/\bar{\nu}\bar{q}}}{\sigma^{\nu\bar{q}/\bar{\nu}q}} = 3. \quad (13.75)$$

By using these quark cross sections and weighing each flavor with the corresponding parton distribution functions in the nucleon, the scattering cross sections in the four-flavor scheme are obtained as:

$$\frac{d^2\sigma^{\nu p}}{dx dy} = \frac{G_F^2 s x}{\pi} (d(x) + s(x) + (1-y^2)(\bar{u}(x) + \bar{c}(x))). \quad (13.76)$$

$$\frac{d^2\sigma^{\bar{\nu} p}}{dx dy} = \frac{G_F^2 s x}{\pi} (\bar{d}(x) + \bar{s}(x) + (1-y^2)(u(x) + c(x))). \quad (13.77)$$

From the isospin symmetry, $u \leftrightarrow d$ for the neutron target, the expressions of the cross section for $\nu_l - n$ and $\bar{\nu}_l - n$ DIS are given by

$$\frac{d^2\sigma^{\nu n}}{dx dy} = \frac{G_F^2 s x}{\pi} (u(x) + s(x) + (1 - y^2)(\bar{d}(x) + \bar{c}(x))), \quad (13.78)$$

$$\frac{d^2\sigma^{\bar{\nu} n}}{dx dy} = \frac{G_F^2 s x}{\pi} (\bar{u}(x) + \bar{s}(x) + (1 - y^2)(d(x) + c(x))). \quad (13.79)$$

Since the fermions discussed here are spin 1/2 particles which can absorb only transversely polarized bosons (W^\pm), the contribution from the longitudinal cross section will be zero. This implies that the Callan–Gross relation, that is, $2xF_1 = F_2$ is also valid in the case of weak interactions. Hence, by using the Callan–Gross relation, the differential cross section given in Eq. (13.66) may be written as ($Q^2 \rightarrow \infty, \nu \rightarrow \infty$):

$$\frac{d^2\sigma^{WI}}{dx dy} = \frac{G_F^2 s}{4\pi} \left[\left(1 + (1 - y)^2\right) F_2^{WI}(x, Q^2) \pm \left(1 - (1 - y)^2\right) xF_3^{WI}(x, Q^2) \right], \quad (13.80)$$

where the terms of order M/E are neglected. On comparing Eqs. (13.76), (13.77), (13.78), and (13.79) with Eq. (13.80), one obtains

$$\begin{aligned} F_2^{\nu_l p}(x) &= 2x[d(x) + s(x) + \bar{u}(x) + \bar{c}(x)], & F_2^{\bar{\nu}_l p}(x) &= 2x[u(x) + c(x) + \bar{d}(x) + \bar{s}(x)], \\ F_2^{\nu_l n}(x) &= 2x[u(x) + s(x) + \bar{d}(x) + \bar{c}(x)], & F_2^{\bar{\nu}_l n}(x) &= 2x[d(x) + c(x) + \bar{u}(x) + \bar{s}(x)], \\ xF_3^{\nu_l p}(x) &= 2x[d(x) + s(x) - \bar{u}(x) - \bar{c}(x)], & xF_3^{\bar{\nu}_l p}(x) &= 2x[u(x) + c(x) - \bar{d}(x) - \bar{s}(x)], \\ xF_3^{\nu_l n}(x) &= 2x[u(x) + s(x) - \bar{d}(x) - \bar{c}(x)], & xF_3^{\bar{\nu}_l n}(x) &= 2x[d(x) + c(x) - \bar{u}(x) - \bar{s}(x)]. \end{aligned}$$

The general expression for the dimensionless nucleon structure functions in terms of parton distribution functions are given by

$$F_2^{WI}(x) = 2 \sum_{i,j} x[e_i^2 q_i(x) + e_j^2 \bar{q}_j(x)]; \quad xF_3^{WI}(x) = 2 \sum_{i,j} x[e_i^2 q_i(x) - e_j^2 \bar{q}_j(x)]. \quad (13.81)$$

In these expressions, i, j run for different flavors of quark/antiquark, and $q_i(x)/\bar{q}_i(x)$ represents the probability density of finding a quark/antiquark with a momentum fraction x . e_i^2 and e_j^2 represent the Cabibbo factors, that is, either $\cos^2 \theta_C$ for the favored transitions or $\sin^2 \theta_C$ for the suppressed transitions. $F_2^{WI}(x)$ and $F_3^{WI}(x)$ are the weak structure functions for neutrino and antineutrino induced processes on proton and neutron targets. These structure functions are obtained by assuming that the CKM matrix is almost unitary in its 2×2 upper left corner or equivalently, that the heavy flavors bottom and top do not mix with the lighter ones.

In the case of an isoscalar target,

$$F_2^{\nu_l(\bar{\nu}_l)N} = \frac{F_2^{\nu_l(\bar{\nu}_l)p} + F_2^{\nu_l(\bar{\nu}_l)n}}{2}, \quad F_3^{\nu_l(\bar{\nu}_l)N} = \frac{F_3^{\nu_l(\bar{\nu}_l)p} + F_3^{\nu_l(\bar{\nu}_l)n}}{2},$$

for which

$$\left. \begin{aligned} F_2^{\nu_l N}(x) &= x[u(x) + \bar{u}(x) + d(x) + \bar{d}(x) + 2s(x) + 2\bar{c}(x)] , \\ F_2^{\bar{\nu}_l N}(x) &= x[u(x) + \bar{u}(x) + d(x) + \bar{d}(x) + 2\bar{s}(x) + 2c(x)] , \\ xF_3^{\nu_l N}(x) &= x[u(x) + d(x) - \bar{u}(x) - \bar{d}(x) + 2s(x) - 2\bar{c}(x)] , \\ xF_3^{\bar{\nu}_l N}(x) &= x[u(x) + d(x) - \bar{u}(x) - \bar{d}(x) + 2c(x) - 2\bar{s}(x)] . \end{aligned} \right\} \quad (13.82)$$

Assuming $s(x) = \bar{s}(x)$ and $c(x) = \bar{c}(x)$, one may write

$$F_2^{\nu_l N}(x) = F_2^{\bar{\nu}_l N}(x) = x[u(x) + \bar{u}(x) + d(x) + \bar{d}(x) + s(x) + \bar{s}(x) + c(x) + \bar{c}(x)] . \quad (13.83)$$

Under the aforesaid assumption, the average of $xF_3^{\nu_l N}(x)$ and $xF_3^{\bar{\nu}_l N}(x)$ gives us the valence quarks measurement, that is,

$$\frac{xF_3^{\nu_l N}(x) + xF_3^{\bar{\nu}_l N}(x)}{2} = x\{u(x) - \bar{u}(x)\} + x\{d(x) - \bar{d}(x)\} = x(u_v(x) + d_v(x)) . \quad (13.84)$$

Hence, through the parity violating structure function $F_{3N}^{WI}(x, Q^2)$, the valence quark distribution inside the nucleon can be directly determined. The difference of $xF_3^{\nu_l N}(x)$ and $xF_3^{\bar{\nu}_l N}(x)$ leads us to

$$\Delta F_{3N}^{WI}(x, Q^2) = xF_3^{\nu_l N}(x) - xF_3^{\bar{\nu}_l N}(x) = 4x\{s(x) - \bar{c}(x)\} , \quad (13.85)$$

which provides information about the strange and charm quarks content in the nucleon.

13.3.1 Relation between electromagnetic and weak structure functions

On comparing the dimensionless nucleon structure function $F_2^{eN}(x)$ given in Eq. (13.29) with $F_2^{\nu_l N}(x)$ given in Eq. (13.82), we can write

$$\begin{aligned} \frac{F_2^{eN}(x)}{F_2^{\nu_l N}(x)} &= \frac{\left[\frac{5}{18} \{u(x) + \bar{u}(x) + d(x) + \bar{d}(x)\} + \frac{4}{9} \{c(x) + \bar{c}(x)\} + \frac{1}{9} \{s(x) + \bar{s}(x)\} \right]}{[u(x) + \bar{u}(x) + d(x) + \bar{d}(x) + s(x) + \bar{s}(x) + c(x) + \bar{c}(x)]} \\ &= \frac{5}{18} \left[1 - \frac{3}{5} \frac{s(x) + \bar{s}(x) - c(x) - \bar{c}(x)}{\sum_i \{q_i(x) + \bar{q}_i(x)\}} \right] . \end{aligned} \quad (13.86)$$

This relation is commonly known as the $\left(\frac{5}{18}\right)$ th rule which confirms the fractional electric charge to the quarks. An important feature of this relation is its sensitivity to the measurement of strange sea quark distribution. In the limit, $s(x) = \bar{s}(x) = c(x) = \bar{c}(x)$:

$$F_2^{eN}(x) \approx \frac{5}{18} F_2^{\nu_l N}(x) = \frac{5}{18} F_2^{\bar{\nu}_l N}(x) . \quad (13.87)$$

Experimental results for the ratio $\frac{5}{18} \left(\frac{F_2^{\nu_l N}(x)}{F_2^{eN}(x)} \right)$ are presented in Figure 13.19, which is found to be in good agreement with the assumptions of the parton model.

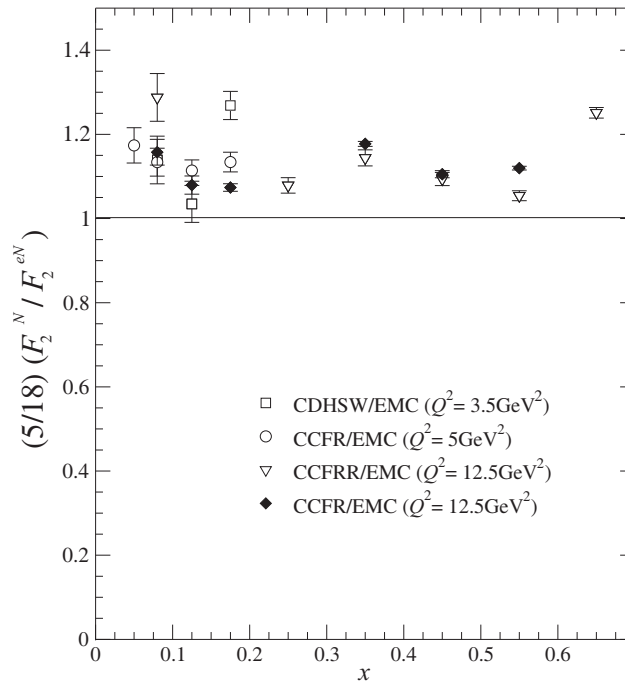


Figure 13.19 Experimental observations for the $\left(\frac{5}{18}\right)$ th rule [564, 565, 566].

13.3.2 Experimental results of charged current total scattering cross section

The total scattering cross sections for the charged current DIS process has been experimentally measured by several experiments such as CCFRR [564], CCFR90 [567], CCFR96 [568], CDHS [569], BEBC-WBB [570], ANL [571], CHARM [572], etc. for neutrino and antineutrino beams, as shown in Figure 13.20. These experiments have been performed on various targets like hydrogen, deuterium, marble, iron, freon, freon-propane, etc. The world average values of total scattering cross section for the neutrino and antineutrino interaction with nucleon/nuclear targets are [573]:

$$\begin{aligned}\sigma^{\nu N}/E_{\nu} &= 0.677 \pm 0.014 \times 10^{-38} \text{cm}^2 \text{GeV}^{-1}, \\ \sigma^{\bar{\nu} N}/E_{\bar{\nu}} &= 0.334 \pm 0.008 \times 10^{-38} \text{cm}^2 \text{GeV}^{-1}.\end{aligned}$$

By integrating Eqs. (13.76), (13.77), (13.78) and (13.79) over x and y between the limits 0 and 1, the expressions of total scattering cross section for an isoscalar nucleon target for neutrino and antineutrino induced processes are obtained as

$$\sigma^{\nu N} = \frac{G_F^2 s}{2\pi} \int x \left(q(x) + \frac{\bar{q}(x)}{3} \right) dx, \quad \sigma^{\bar{\nu} N} = \frac{G_F^2 s}{2\pi} \int x \left(\frac{q(x)}{3} + \bar{q}(x) \right) dx. \quad (13.88)$$

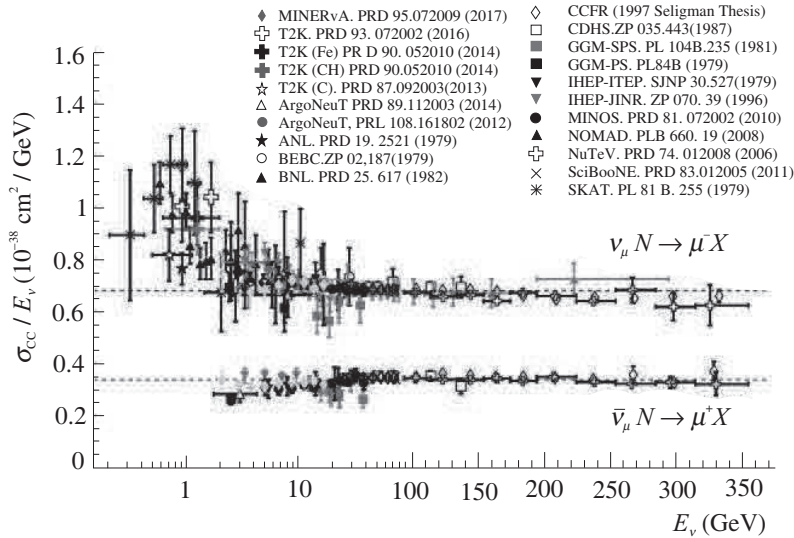


Figure 13.20 Charged current total cross section for $\nu_l - N$ and $\bar{\nu}_l - N$ processes [117].

Through the total scattering cross section, one may directly determine the total momentum carried by all the quarks and antiquarks, that is,

$$\int x(q(x) + \bar{q}(x)) dx = \frac{3\pi}{2 G_F^2 s} (\sigma^{\nu N} + \sigma^{\bar{\nu} N}) \quad (13.89)$$

and the fraction carried by the antiquarks as:

$$\frac{\int x\bar{q}(x) dx}{\int x(q(x) + \bar{q}(x)) dx} = \frac{1}{2} \left(\frac{3\sigma^{\bar{\nu} N} - \sigma^{\nu N}}{\sigma^{\nu N} + \sigma^{\bar{\nu} N}} \right), \quad (13.90)$$

which are experimentally found to be [572]:

$$\begin{aligned} \int x(q(x) + \bar{q}(x)) dx &= 0.492 \pm 0.006 \pm 0.019, \\ \frac{\int x\bar{q}(x) dx}{\int x(q(x) + \bar{q}(x)) dx} &= 0.154 \pm 0.005 \pm 0.011. \end{aligned}$$

From these equations, it may be noticed that in the limits of high Q^2 and ν , charged partons carry only 50% of the nucleon's momentum and among them, antiquarks carry 15% of the charged partons momentum; the remaining 50% of the momentum is carried by the gluon.

13.4 Deep Inelastic Neutral Current $\nu_l/\bar{\nu}_l - N$ Scattering

The differential scattering cross section for (anti)neutrino induced neutral current (NC) deep inelastic scattering processes which are mediated by Z^0 boson (as shown in Figure 13.21) is given by

$$\frac{d^2\sigma_N^{WI}}{dx dy} = \frac{G_F^2}{2\pi} \left[xy^2 F_{1N}^{WI,NC}(x, Q^2) + \left(1 - y - \frac{Mxy}{2E_l}\right) F_{2N}^{WI,NC}(x, Q^2) \pm xy \left(1 - \frac{y}{2}\right) F_{3N}^{WI,NC}(x, Q^2) \right], \quad (13.91)$$

where $F_{iN}^{WI,NC}(x, Q^2)$; ($i = 1 - 3$) are the neutral current weak structure functions. In the case of neutral current weak interactions, both neutrinos and antineutrinos couple to all the quarks and antiquarks. There is no difference between the neutral current structure functions $F_{2N}^{WI,NC}(x, Q^2)$ and $x F_{3N}^{WI,NC}(x, Q^2)$ for neutrino and antineutrino induced processes. In the

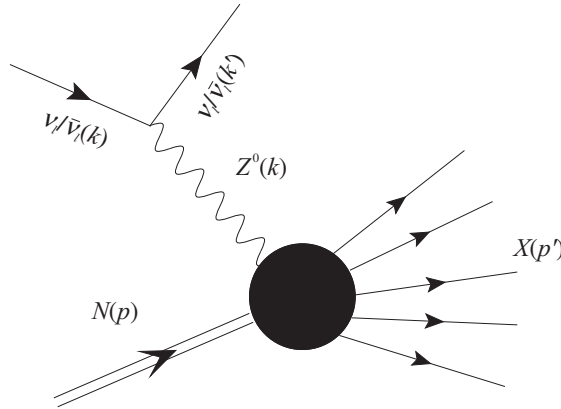


Figure 13.21 Feynman diagram for the neutral current $\nu_l(\bar{\nu}_l) - N$ DIS process.

expression of the differential cross section, the term with $x F_{3N}^{WI,NC}(x, Q^2)$ has opposite signs for the neutrino (+ve) and the antineutrino (−ve). The neutral current structure functions $F_{2N}^{WI,NC}(x, Q^2)$ and $x F_{3N}^{WI,NC}(x, Q^2)$ are written in terms of PDFs as:

$$F_2^{\nu_l(\bar{\nu}_l)p \rightarrow \nu_l(\bar{\nu}_l)X}(x) = 2x \left([(e_L^u)^2 + (e_R^u)^2] \cdot [u(x) + \bar{u}(x) + c(x) + \bar{c}(x)] + [(e_L^d)^2 + (e_R^d)^2] \cdot [d(x) + \bar{d}(x) + s(x) + \bar{s}(x)] \right) \quad (13.92)$$

$$x F_3^{\nu_l(\bar{\nu}_l)p \rightarrow \nu_l(\bar{\nu}_l)X}(x) = 2x \left([(e_L^u)^2 - (e_R^u)^2] \cdot [u(x) - \bar{u}(x) + c(x) - \bar{c}(x)] + [(e_L^d)^2 - (e_R^d)^2] \cdot [d(x) - \bar{d}(x) + s(x) - \bar{s}(x)] \right), \quad (13.93)$$

where for the neutron target, $u(x) \rightarrow d(x)$, $\bar{u}(x) \rightarrow \bar{d}(x)$ and vice versa. e_L^q and e_R^q are the left- and right-handed coupling constants. These coupling constants are determined by a

combination of the weak isospin's longitudinal component (I_3) and the electric charge (Q_e) of the interacting quarks, rather than by their electric charges alone, as in charged current interactions. These coupling constants are also functions of $\sin^2 \theta_W$:

$$e_L^q = I_3^q - Q_e^q \sin^2 \theta_W, \quad e_R^q = -Q_e^q \sin^2 \theta_W. \quad (13.94)$$

Using the value of I_3 and Q_e for quarks, we get:

$$\begin{aligned} (e_L^u)^2 &= \left(+\frac{1}{2} - \frac{2}{3} \sin^2 \theta_W \right)^2, & (e_L^d)^2 &= \left(-\frac{1}{2} + \frac{1}{3} \sin^2 \theta_W \right)^2 \\ (e_R^u)^2 &= \left(-\frac{2}{3} \sin^2 \theta_W \right)^2, & (e_R^d)^2 &= \left(+\frac{1}{3} \sin^2 \theta_W \right)^2. \end{aligned}$$

By using the charged current and neutral current (anti)neutrino–nucleon scattering cross sections, one may obtain the standard model parameter $\sin^2 \theta_W$, coupling strength of weak neutral current to strange and down quarks and the ratio $R_L^{WI}(x, Q^2) = \frac{\sigma_L^{WI}(x, Q^2)}{\sigma_T^{WI}(x, Q^2)}$ which provides information about the violation of the Callan–Gross relation. The results for the differential scattering cross section by the CHARM collaboration [574] are shown in Figure 13.22 for (anti)neutrino scattering in charged and neutral current induced processes.

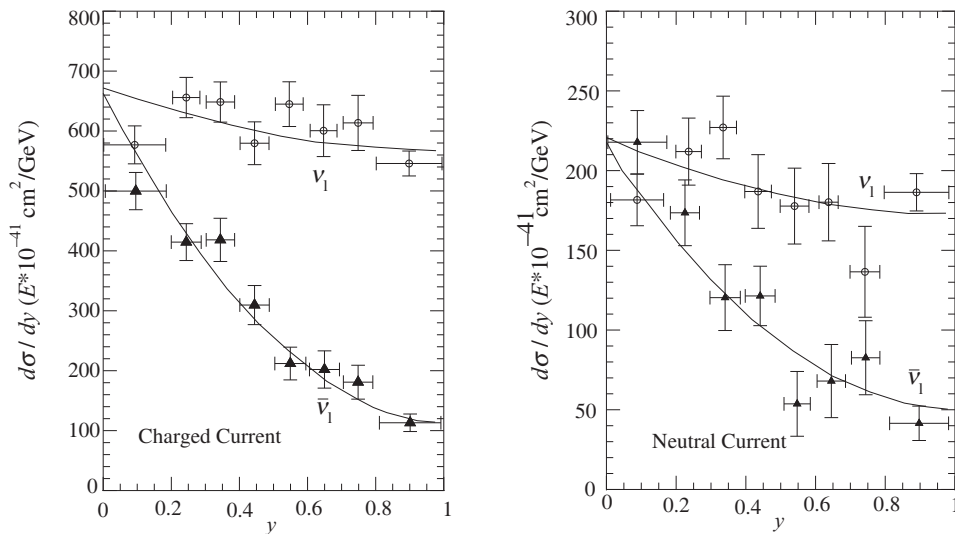


Figure 13.22 Charged and neutral current (anti)neutrino differential cross sections by CHARM collaboration [574].

Now, in order to obtain the weak mixing angle, the differential scattering cross sections for the charged and neutral current induced processes is written in terms of parton distribution functions for an isoscalar nucleon target as

$$\frac{d^2 \sigma_{\nu N}^{CC}}{dx dy} = \frac{G_F^2 s x}{2\pi} [\{q(x) + (1-y)^2 \bar{q}(x)\} + \{s(x) - c(x)\} + (1-y)^2 \{\bar{c}(x) - \bar{s}(x)\}] ,$$

$$\begin{aligned}
\frac{d^2\sigma_{\bar{\nu}N}^{CC}}{dx dy} &= \frac{G_F^2 s x}{2\pi} [\{\bar{q}(x) + (1-y)^2 q(x)\} + \{\bar{s}(x) - \bar{c}(x)\} + (1-y)^2 \{c(x) - s(x)\}] , \\
\frac{d^2\sigma_{\nu N}^{NC}}{dx dy} &= \frac{G_F^2 s x}{2\pi} [\{(e_L^u)^2 + (e_L^d)^2\} \{q(x) + (1-y)^2 \bar{q}(x)\} \\
&\quad + \{(e_R^u)^2 + (e_R^d)^2\} \{\bar{q}(x) + q(x)(1-y)^2\} \\
&\quad + \{(e_L^u)^2 - (e_L^d)^2 + (1-y)^2 [(e_R^u)^2 - (e_R^d)^2]\} (c(x) - s(x)) \\
&\quad + \{(e_R^u)^2 - (e_R^d)^2 + (1-y)^2 [(e_L^u)^2 - (e_L^d)^2]\} (\bar{c}(x) - \bar{s}(x))] , \quad (13.95)
\end{aligned}$$

$$\begin{aligned}
\frac{d^2\sigma_{\bar{\nu}N}^{NC}}{dx dy} &= \frac{G_F^2 s x}{2\pi} [\{(e_R^u)^2 + (e_R^d)^2\} \{q(x) + (1-y)^2 \bar{q}(x)\} \\
&\quad + \{(e_L^u)^2 + (e_L^d)^2\} \{\bar{q}(x) + q(x)(1-y)^2\} \\
&\quad + \{(e_R^u)^2 - (e_R^d)^2 + (1-y)^2 [(e_L^u)^2 - (e_L^d)^2]\} (c(x) - s(x)) \\
&\quad + \{(e_L^u)^2 - (e_L^d)^2 + (1-y)^2 [(e_R^u)^2 - (e_R^d)^2]\} (\bar{c}(x) - \bar{s}(x))] , \quad (13.96)
\end{aligned}$$

where $q(x) = u(x) + d(x) + c(x) + s(x)$ and $\bar{q}(x) = \bar{u}(x) + \bar{d}(x) + \bar{c}(x) + \bar{s}(x)$. The ratio of scattering cross sections

$$R_{\pm} = \frac{(\sigma_{\nu N}^{NC} \pm \sigma_{\bar{\nu}N}^{NC})}{(\sigma_{\nu N}^{CC} \pm \sigma_{\bar{\nu}N}^{CC})}$$

is defined by taking into account only two flavors of quark, that is, up and down to simplify the numerical calculations and is obtained as

$$\begin{aligned}
R_{\pm} &= \frac{\{(e_L^u)^2 + (e_L^d)^2 \pm (e_R^u)^2 + (e_R^d)^2\} \{1 \pm (1-y)^2\} \{u(x) + d(x)\} \pm \{\bar{u}(x) + \bar{d}(x)\}}{\{1 \pm (1-y)^2\} \{u(x) + d(x)\} \pm \{\bar{u}(x) + \bar{d}(x)\}} \\
&= \{(e_L^u)^2 + (e_L^d)^2\} \pm \{(e_R^u)^2 + (e_R^d)^2\}. \quad (13.97)
\end{aligned}$$

By substituting the values of the left- and right-handed couplings (Eq. (13.94)), one obtains

$$R_+ = \frac{1}{2} - \sin^2 \theta_W + \frac{10}{9} \sin^4 \theta_W, \quad R_- = \frac{1}{2} - \sin^2 \theta_W, \quad (13.98)$$

where Eq. (13.98) is known as the Paschos–Wolfenstein relation through which the weak mixing angle $\sin^2 \theta_W$ is extracted.

Moreover, the ratio of neutral to charged current scattering cross section for the neutrino (R_{ν}) and the antineutrino ($R_{\bar{\nu}}$) induced processes are obtained as

$$R_{\nu} = \frac{\sigma_{\nu N}^{NC}}{\sigma_{\nu N}^{CC}} = \{(e_L^u)^2 + (e_L^d)^2\} + \kappa(x) \{(e_R^u)^2 + (e_R^d)^2\}, \quad (13.99)$$

$$R_{\bar{\nu}} = \frac{\sigma_{\bar{\nu}N}^{NC}}{\sigma_{\bar{\nu}N}^{CC}} = \{(e_L^u)^2 + (e_L^d)^2\} + \kappa^{-1}(x) \{(e_R^u)^2 + (e_R^d)^2\}, \quad (13.100)$$

$$\text{where } \kappa(x) = \frac{\{\bar{q}(x) + (1-y)^2 q(x)\}}{\{q(x) + (1-y)^2 \bar{q}(x)\}}. \quad (13.101)$$

This ratio measures the relative strength of the sea and valence quarks contributions. After simplification, R_ν and $R_{\bar{\nu}}$ may also be written as

$$\left. \begin{aligned} R_\nu &= \frac{1}{2} - \sin^2 \theta_W + \frac{5}{9}(1 + \kappa(x)) \sin^4 \theta_W, \\ R_{\bar{\nu}} &= \frac{1}{2} - \sin^2 \theta_W + \frac{5}{9}(1 + \kappa^{-1}(x)) \sin^4 \theta_W. \end{aligned} \right\} \quad (13.102)$$

These ratios have been obtained by several experimental collaborations; for example, the measured values are

$$\begin{aligned} R_\nu &= 0.3072 \pm 0.0025 \pm 0.0020 \quad \text{CDHS [575]}, \\ R_\nu &= 0.3098 \pm 0.0031 \quad \text{CHARM [576]}, \\ R_{\bar{\nu}} &= 0.363 \pm 0.015 \quad \text{CDHS [577]}. \end{aligned}$$

The value of R_ν has been found to be more sensitive to the predicted value of weak mixing angle by the standard model in comparison to $R_{\bar{\nu}}$. The experimental values of $\sin^2 \theta_W$ from the different collaborations are given by

$$\begin{aligned} \sin^2 \theta_W &= 0.225 \pm 0.005(\text{exp.}) \pm 0.003(\text{theor.}) \pm 0.013(m_c - 1.5 \text{ GeV}/c^2), \text{CDHS [575]} \\ &= 0.236 \pm 0.005(\text{exp.}) \pm 0.003(\text{theor.}) \pm 0.012(m_c - 1.5 \text{ GeV}/c^2), \text{CHARM [576]} \\ &= 0.2233 \pm 0.0008 \pm 0.0004, \quad \text{CDF [578]}, \end{aligned}$$

where m_c is the mass of the charm quark, while the world average value of $\sin^2 \theta_W$ is [579]

$$\sin^2 \theta_W = 0.23122(4) \pm 0.00017.$$

Till now, the DIS processes induced by the charged lepton and (anti)neutrino has been discussed. In the next section, the perturbative as well as the non-perturbative QCD corrections will be discussed. These corrections are important for the precise determination of the nucleon structure functions.

13.5 QCD Corrections

13.5.1 Modified parton model

In the naive parton model, the structure functions were assumed to be the function of a dimensionless variable x , that is,

$$\begin{aligned} F_{1N}(x, Q^2) &\xrightarrow[Q^2 \rightarrow \infty, \nu \rightarrow \infty]{x \rightarrow \text{finite}} F_{1N}(x), \\ F_{2N}(x, Q^2) &\xrightarrow[Q^2 \rightarrow \infty, \nu \rightarrow \infty]{x \rightarrow \text{finite}} F_{2N}(x). \end{aligned}$$

However, QCD predicts that if one increases the four-momentum transfer squared Q^2 , then each quark is found to be surrounded by a number of partons. Therefore, the effective number of resolved partons carrying a fraction of the nucleon's momentum increases with the increase

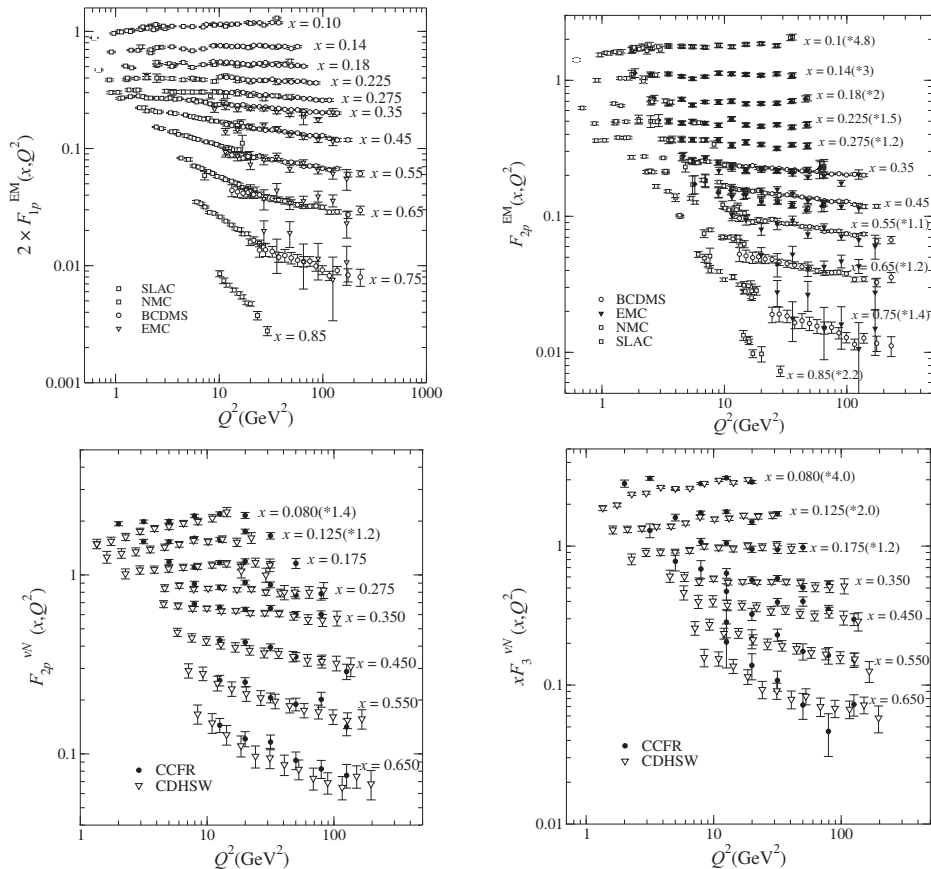


Figure 13.23 Experimental results of nucleon structure functions for (i) Top panel: electromagnetic interaction induced DIS process [548, 557, 558, 559, 560], (ii) Bottom panel: weak interaction induced DIS process [561, 562].

in Q^2 or in other words, parton distribution functions show Q^2 dependence leading to the phenomenon of scaling violation. This phenomenon was confirmed by several electron scattering experiments such as EMC, NMC, BCDMS, etc. [557, 558, 559].

In Figure 13.23 (top panel), the experimental results are shown for the electromagnetic nucleon structure functions in a wide range of x and Q^2 . Later, scaling violation was also observed in (anti)neutrino scattering experiments such as CDHSW [561] and CCFR [562] for which the results are shown in Figure 13.23 (bottom panel). From these figures, it may be observed that with the increase in x and Q^2 , the structure functions fall down, while for lower x and Q^2 , there is a rise. This behavior of structure functions show scaling breakdown.

In perturbative QCD (pQCD), partons present inside the nucleon interact among themselves via the gluon exchange; the contribution from the gluons is responsible for the Q^2 dependence of nucleon structure functions. For example, in the case of electromagnetic interactions, $\gamma^* q \rightarrow qg$ and $\gamma^* g \rightarrow q\bar{q}$ are the possible channels, which are depicted in Figure 13.24 [400]. Generally, the Q^2 dependence of structure functions is determined by evolving the Q^2

dependent parton densities using the Dokshitzer–Gribov–Lipatov–Altarelli–Parisi (DGLAP) evolution equation [580] which is too technical to be included here. Since the structure functions are a combination of parton density distribution functions, it is important to understand their behavior in the entire kinematic region of x and Q^2 .

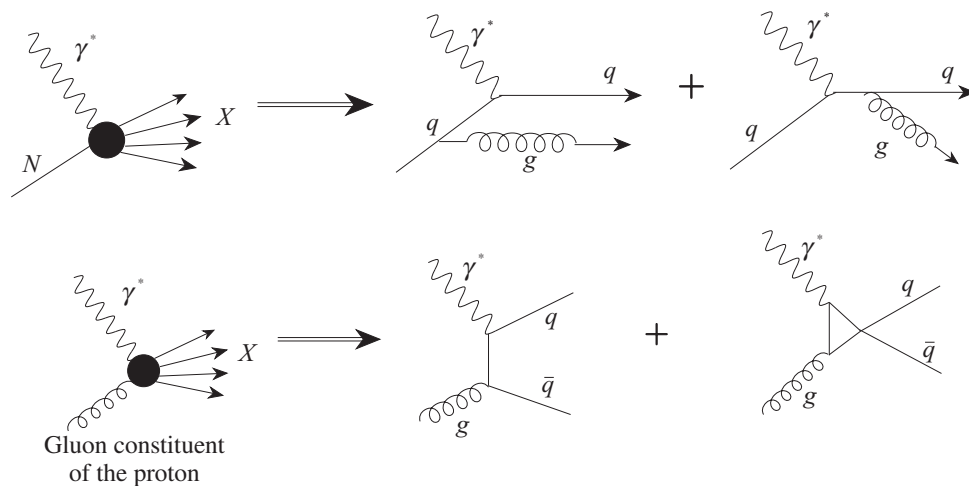


Figure 13.24 Diagrammatic representation of (i) upper panel: the process $\gamma^* q \rightarrow qg$ and (ii) lower panel: the process $\gamma^* g \rightarrow q\bar{q}$ [400].

Extraction of parton densities

Through perturbative QCD, the Q^2 evolution of parton distribution functions can be inferred but their x dependence cannot be predicted. Therefore, it is convenient to make a suitable choice of analytic parameterization consistent with the Q^2 dependence predicted by pQCD. Beyond the leading order, an exact analytic expression valid for a wide range of x and Q^2 , consistent with the pQCD is very difficult to be found. Therefore, DGLAP equations are generally used to extract the parton densities beyond the leading order; they are given by

$$\frac{\partial}{\partial \ln Q^2} \begin{pmatrix} q_i(x, Q^2) \\ g(x, Q^2) \end{pmatrix} = \frac{\alpha_s(Q^2)}{2\pi} \sum_j \int_x^1 \frac{dz}{z} \begin{pmatrix} P_{qi q_j}(\frac{x}{y}, \alpha_s(Q^2)) & P_{qi g}(\frac{x}{y}, \alpha_s(Q^2)) \\ P_{gq_j}(\frac{x}{y}, \alpha_s(Q^2)) & P_{gg}(\frac{x}{y}, \alpha_s(Q^2)) \end{pmatrix} \begin{pmatrix} q_j(y, Q^2) \\ g(y, Q^2) \end{pmatrix}, \quad (13.103)$$

where $\alpha_s(Q^2)$ is the strong coupling constant, $q(x, Q^2)$ and $g(x, Q^2)$ are the quark and gluon density distribution functions, and $P_{ij}(\frac{x}{y}, \alpha_s(Q^2))$ ($i, j = q$ or g) are the splitting functions which are expanded in a power series of $\alpha_s(Q^2)$. The splitting function describes the probability for the splitting of a parton into two other partons having a smaller momentum fraction than the parent parton, for example, $P_{qi q_j}$ gives the probability of splitting of a quark into a pair of quarks and a gluon. All the possibilities for the splitting of a parton at leading order are shown in Figure 13.25. The evolution equations explain that the valence quarks are surrounded by a number of virtual particles which are continuously getting absorbed and emitted. For the extraction of parton densities using the DGLAP equation, the analytic shape is assumed to be valid at an arbitrary but sufficiently large value of Q^2 (i.e., small $\alpha_s(Q^2)$) so that perturbative

calculations can be applicable. Then through the DGLAP equation, the evolution of parton densities is performed up to different values of Q^2 . The parton densities are convoluted over the coefficient functions (which are discussed in the next subsection) to predict the nucleon structure functions. By fitting the predicted structure functions to the available experimental

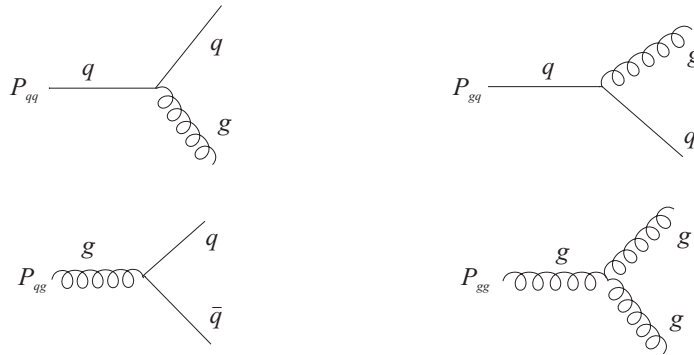


Figure 13.25 Diagrammatic representation of splitting functions.

data, the input parameters are determined. In the literature, a large amount of high statistics experimental data are available for the deep inelastic scattering processes such as $e^\pm - N$, $e^\pm - A$, $\mu^\pm - N$, $\mu^\pm - A$, $\nu_l - A$, etc., which are used to extract parton densities with high accuracy. However, besides DIS, the Drell–Yan (DY) process with hadronic probes like $p - A$, $\pi^\pm - A$, $d - A$, etc., are also used to obtain information about parton densities. Various groups have found the global fits of parton density distribution by using the available experimental data, for example, CTEQ [551], MSTW [550], GJR [549], MMHT [552]. Thus, using this procedure, the PDFs have been obtained in the whole range of x and at any value of Q^2 by interpolation.

The probability of the gluon emission is related to the strong coupling constant $\alpha_s(Q^2)$, which varies with the value of Q^2 . For example, in the limit of $Q^2 \rightarrow \infty$, the strong coupling constant $\alpha_s(Q^2)$ becomes very small and, therefore, the higher order terms can be neglected in comparison to the leading order (LO) terms. However, for a finite value of Q^2 , $\alpha_s(Q^2)$ is large and higher order terms such as next-to-leading order (NLO), and next-to-next-to-leading order (NNLO), etc., give a significant contribution. In the next section, the evolution of PDFs at NLO is discussed.

13.5.2 NLO evolution

For a precise determination of the nucleon structure functions, in the limit of finite Q^2 , the next-to-leading order (NLO) followed by the next-to-next-to-leading order (NNLO) terms should be taken into account. In Figure 13.26, the parton density distribution functions are shown at LO, NLO, and NNLO for $Q^2 = 2 \text{ GeV}^2$. For example these results are obtained by using the MMHT PDFs parameterization [552]. One may observe that while we go from LO to NLO, there is a significant difference in PDFs; however, the difference is comparatively smaller between NLO and NNLO. In literature, different approaches are available for the QCD

corrections at NLO and NNLO for the evolution of PDFs, which are used to obtain the nucleon structure function, for example, as discussed in Refs. [581, 582, 583, 584, 585, 586, 587]. Here, we are demonstrating in brief the basic concept of performing evolution at NLO.

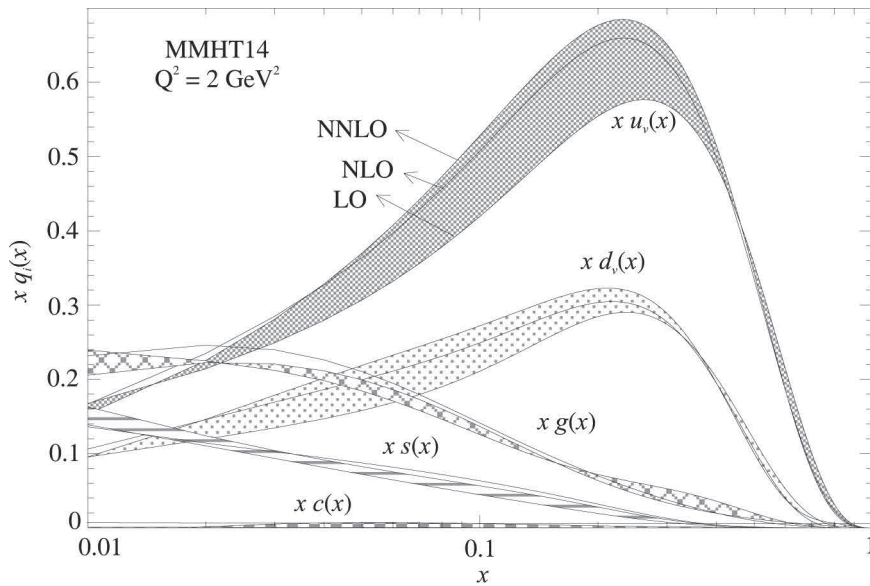


Figure 13.26 Evolution of parton density distribution functions using MMHT PDFs parameterization [552] from leading order to next-to-next-leading order at $Q^2 = 2 \text{ GeV}^2$.

The nucleon structure functions may be expressed in terms of the convolution of coefficient function C_f with the density distribution of partons (f) inside the nucleon. The parton coefficient functions are generally expressed as

$$C_f(x, Q^2) = C_f^{(0)} + \frac{\alpha_s(Q^2)}{2\pi} C_f^{(1)} + \left(\frac{\alpha_s(Q^2)}{2\pi} \right)^2 C_f^{(2)} + \dots \quad (13.104)$$

The nucleon structure function, for example, $F_{2N}(x)$ is written in terms of the coefficient function as

$$x^{-1} F_{2N}^{EM, WI}(x) = \sum_{f=q, g} C_2^{(n)}(x) \otimes f(x), \quad (13.105)$$

where superscript $n = 0, 1, 2, \dots$ for $N^{(n)}\text{LO}$ and the symbol \otimes is the Mellin convolution.

$$C_f(x) \otimes f(x) = \int_x^1 C_f(y) f\left(\frac{x}{y}\right) \frac{dy}{y}. \quad (13.106)$$

This Mellin convolution turns into a simple multiplication in the Mellin space. The expression for $F_{2N}(x)$ is simplified as [581]:

$$x^{-1} F_{2N}^{EM, WI}(x) = c_{2, ns}^{(n)}(x) \otimes q_{ns}(x) + \langle e^2 \rangle (c_{2, q}^{(n)}(x) \otimes q_s(x) + c_{2, g}^{(n)}(x) \otimes g(x)),$$

where $\langle e^2 \rangle$ is the average charge of partons; $q_s(x)$, $q_{ns}(x)$ are the singlet and the non-singlet quark distributions; and $g(x)$ is the gluon distribution. $c_{2,ns}(x)$ is the coefficient function for the non-singlet and $c_{2,q}^{(n)}(x)$ and $c_{2,g}^{(n)}(x)$ are the coefficient functions for the singlet quark and gluon, respectively. For a three-flavor scheme, $\langle e^2 \rangle$ is obtained as:

$$\langle e^2 \rangle = \frac{e_u^2 + e_d^2 + e_s^2}{3} = \frac{1}{3} \left(\frac{4}{9} + \frac{1}{9} + \frac{1}{9} \right) = \frac{2}{9},$$

while for the four-flavor scheme,

$$\langle e^2 \rangle = \frac{e_u^2 + e_d^2 + e_c^2 + e_s^2}{3} = \frac{1}{4} \left(\frac{4}{9} + \frac{1}{9} + \frac{4}{9} + \frac{1}{9} \right) = \frac{5}{18}.$$

The singlet and non-singlet quark distributions in the four-flavor scheme are given by

$$\begin{aligned} q_s(x) &= u(x) + \bar{u}(x) + d(x) + \bar{d}(x) + s(x) + \bar{s}(x) + c(x) + \bar{c}(x) \\ q_{ns}(x) &= F_{2N}^{EM,WI}(x) - \langle e^2 \rangle q_s, \end{aligned}$$

with $\langle e^2 \rangle = \frac{5}{18}$ for the electromagnetic interaction and $\langle e^2 \rangle = 1$ for the weak interaction (see the discussion followed by Eq. (13.81)). At the leading order, the coefficient functions for quarks and gluons are, respectively $C_{2,q}^{(0)}(x) = \delta(1-x)$ and $C_{2,g}^{(0)}(x) = 0$; while at NLO, they are written as [581]:

$$C_{q,2}^{(1)}(x) = c_{2,ns}^{(1)}(x) + c_{2,q}^{(1)}(x), \quad C_{g,2}^{(1)}(x) = c_{2,g}^{(1)}(x). \quad (13.107)$$

For the detailed expressions of the coefficient functions, see Ref. [581]. The expression for the weak structure function $F_{3N}^{WI}(x)$ in terms of the coefficient function and parton density distribution function is given by [588]:

$$F_{3N}^{WI}(x) = \sum_{f=q,g} C_3(x) \otimes f(x) = C_3(x) \otimes q_v(x),$$

where $q_v(x)$ is the valence quark distribution and $C_3(x)$ is the coefficient function for $F_{3N}^{WI}(x)$. It is important to point out that coefficient functions for the longitudinal structure function $F_{LN}^{EM,WI}(x, Q^2)$ are suppressed by a power of $\frac{\alpha_s(Q^2)}{2\pi}$ as compared to the case of $F_{2N}^{EM,WI}(x, Q^2)$ and $F_{3N}^{WI}(x, Q^2)$. For the detailed discussion, please see Refs. [581], [582], [588] and [589]. The parton distributions are process independent but they depend on the target. Therefore, the incorporation of the target mass gives rise to new terms that lead to additional power corrections of kinematical origin. This is known as the target mass correction (TMC) effect. In the next section, the target mass correction effect, which is taken into account for better determination of the nucleon structure functions, will be discussed.

13.5.3 TMC effect

The target mass correction (TMC) effect is a non-perturbative effect which comes into the picture at low Q^2 , where perturbation theory is not valid. The TMC effect is significant

at low Q^2 and high x , which is important to determine the distribution of valence quarks. Unfortunately, this kinematic region has not been explored much, unlike the region of high Q^2 and low x . The TMC effect is also known as ‘kinematic higher twist effect’. In 1976, Georgi and Politzer determined the target mass corrections to electroweak structure functions, using the operator product expansion (OPE) at the leading order of QCD [590].

At a finite value of Q^2 , the mass of the target nucleon and the quark masses modify the Bjorken variable x with the light cone momentum fraction. For the massless quarks, the parton light cone momentum fraction is given by the Nachtmann variable (ξ) which is defined as [591]:

$$\xi = \frac{2x}{1 + \sqrt{1 + \frac{4M^2x^2}{Q^2}}}. \quad (13.108)$$

Notice that ξ depends only on the hadronic mass. In the case of massive quarks, ξ gets modified to the slow rescaling variable $\bar{\xi}$ which is given by [591]

$$\bar{\xi} = \xi \left(1 + \frac{m_q^2}{Q^2} \right), \quad (13.109)$$

where m_q is the quark mass. It is noticeable that the Nachtmann variable corrects the Bjorken variable for the effects of hadronic mass while the generalized variable $\bar{\xi}$ further corrects ξ for

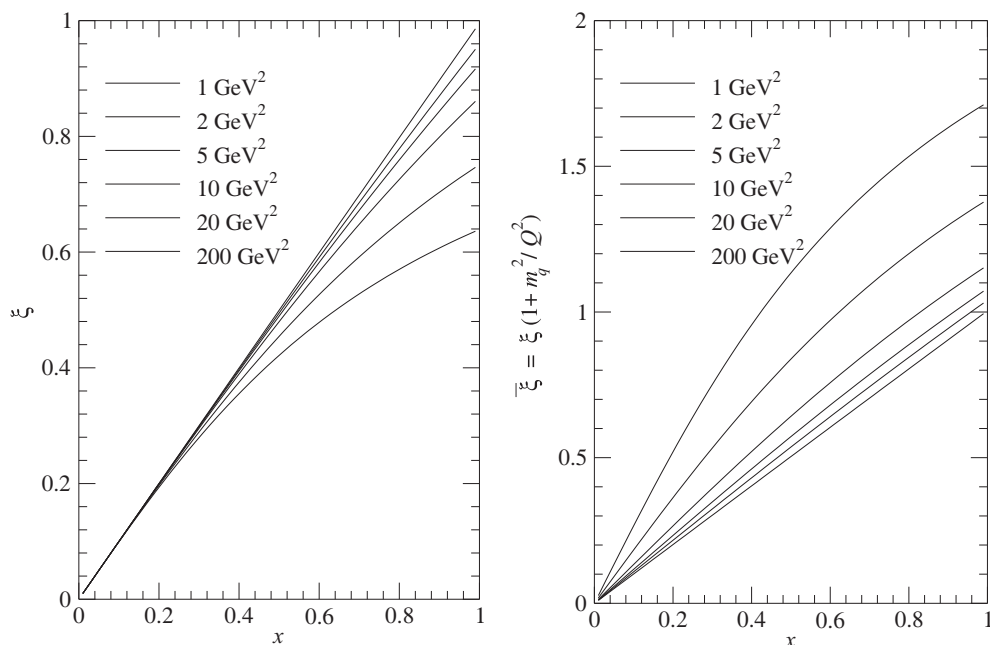


Figure 13.27 Nachtmann variable ξ and slow rescaling variable $\bar{\xi}$ vs. x are shown at different values of Q^2 .

the effects of the partonic masses [591]. The dependence of ξ and $\bar{\xi}$ on the Bjorken variable x and four momentum transfer squared Q^2 is shown in Figure 13.27. From the figure, one can observe that for the low values of momentum transfer squared, both the Nachtmann variable and the slow rescaling variable significantly deviate from the Bjorken variable, specially at high x . However, in the case of high momentum transfer squared ($Q^2 \gg m_q^2$), quark masses are negligible; hence, these variables get reduced to the Bjorken variable, that is

$$\xi \xrightarrow{Q^2 \gg m_q^2} x \quad \text{and} \quad \bar{\xi} \xrightarrow{Q^2 \gg m_q^2} x. \quad (13.110)$$

The effect of target mass corrections obtained in the different approaches such as operator product expansion [591], the approach discussed by Ellis–Furmanski–Petronzio [592] and ξ –scaling [593, 594] are shown in Figure 13.28 at $Q^2 = 2 \text{ GeV}^2$. From the figure, it can be observed that TMC effect dominates in the region of high x and low Q^2 .

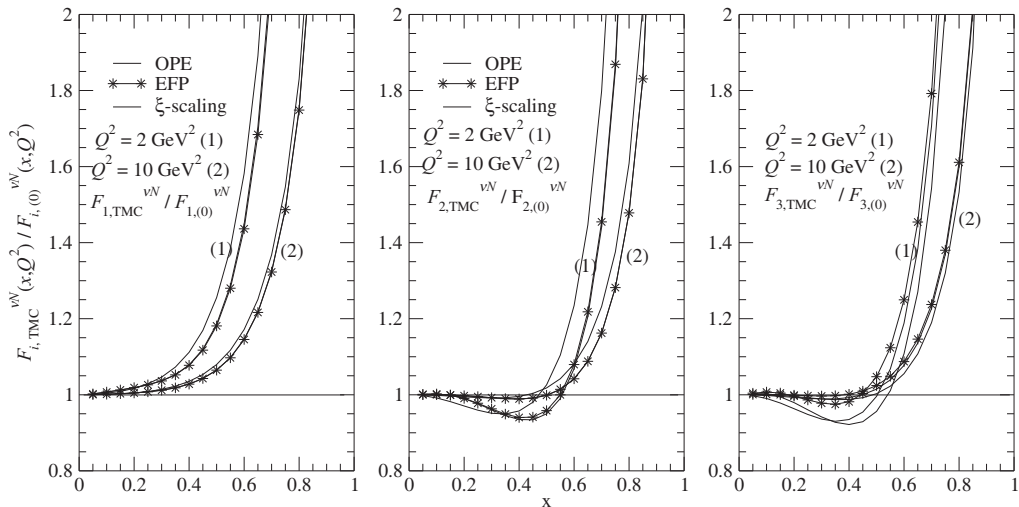


Figure 13.28 Ratio of target mass corrected weak structure functions to the structure functions without TMC by using MMHT PDFs parameterization [552] at NLO for $Q^2 = 2 \text{ GeV}^2$. These results are obtained by using Refs. [591, 592, 593, 594].

For example, following the works of Schienbein et al. [591], the structure functions with the TMC effect are given by

$$\left. \begin{aligned} F_{1N}^{TMC}(x, Q^2) &\approx \frac{x}{\xi\gamma} F_{1N}(\xi) (1 + 2r(1 - \xi)^2), \\ F_{2N}^{TMC}(x, Q^2) &\approx \frac{x^2}{\xi^2\gamma^3} F_{2N}(\xi) (1 + 6r(1 - \xi)^2), \\ F_{3N}^{TMC}(x, Q^2) &\approx \frac{x}{\xi\gamma^2} F_{3N}(\xi) (1 - r(1 - \xi) \ln \xi), \end{aligned} \right\} \quad (13.111)$$

where $r = \frac{\mu x \xi}{\gamma}$, $\mu = \left(\frac{M}{Q}\right)^2$ and $\gamma = \sqrt{1 + \frac{4M^2 x^2}{Q^2}}$, respectively. Similar to the TMC effect, there is another non-perturbative effect known as the ‘higher twist effect’ or ‘dynamical higher twist effect’, which is described in brief in the following section.

13.5.4 Higher twist effect

The possible sources of higher twist effect are QCD radiative corrections, final state interactions, finite target mass, etc., while in perturbative QCD, renormalons are responsible for this effect. Higher twist (HT) effect is a dynamical effect arising due to multiparton correlations. Therefore, this effect involves the interactions of struck quark with other quarks via the exchange of gluon; it is suppressed by the power of $\left(\frac{1}{Q^2}\right)^n$, where $n = 1, 2, \dots$. The higher twist effect is pronounced in the region of low Q^2 and high x , like the TMC effect, but is negligible for high Q^2 and low x .

For lower values of Q^2 , at a few GeV or less, non-perturbative phenomena become important for a precise modeling of cross sections, in addition to higher-order QCD corrections. In the formalism of the operator product expansion (OPE), unpolarized structure functions can be expressed in terms of powers of $1/Q^2$ (power corrections):

$$F_i(x, Q^2) = F_i^{\tau=2}(x, Q^2) + \frac{H_i^{\tau=4}(x)}{Q^2} + \frac{H_i^{\tau=6}(x)}{Q^4} + \dots; \quad i = 1, 2, 3, \quad (13.112)$$

where the first term ($\tau = 2$) is known as the twist-two or leading twist (LT) term, and corresponds to the scattering off a free quark. This term obeys the Altarelli-Parisi equation and is expressed in terms of PDFs. It is responsible for the evolution of structure functions via perturbative QCD $\alpha_s(Q^2)$ corrections. The HT terms with $\tau = 4, 6, \dots$ reflect the strength of multiparton correlations (qq and qg). The HT corrections spoil the QCD factorization; therefore, one should consider their impact on the PDFs extracted in the analysis of low Q data.

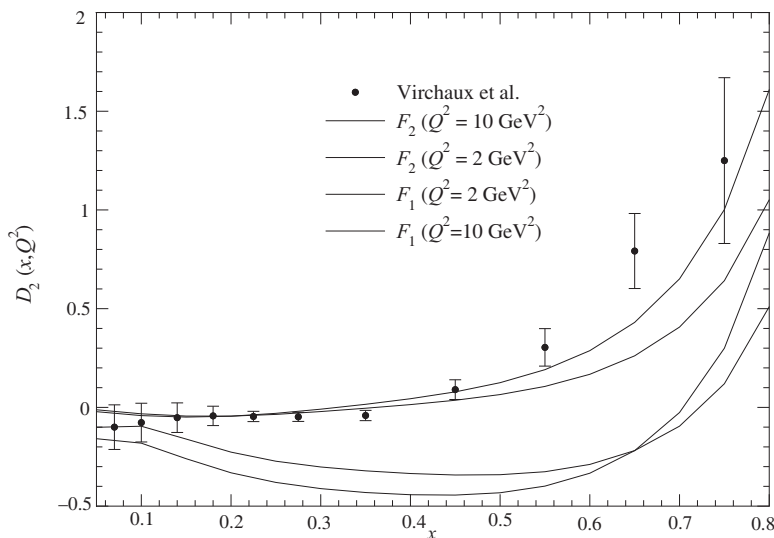


Figure 13.29 Twist-4 coefficient in the renormalon approach [595] for $F_1^{\text{EM}}(x, Q^2)$ and $F_2^{\text{EM}}(x, Q^2)$ obtained by using MMHT PDFs parameterization [552] at NLO for $Q^2 = 2 \text{ GeV}^2$ and 10 GeV^2 . The results are compared with the results of Virchaux et al. [596].

Due to their non-perturbative origin, current models can only provide a qualitative description for such contributions, which are usually determined via reasonable assumptions from data. In Figure 13.29, the twist-4 coefficient function obtained by following the renormalon approach [595] is shown and compared with the phenomenological coefficient function of Virchaux et al. [596]. From the figure, it may be observed that the effect of higher twist corrections are different for $F_1^{\text{EM}}(x, Q^2)$ and $F_2^{\text{EM}}(x, Q^2)$ in the entire region of x . Furthermore, to show the Q^2 dependence of the coefficient function $D_2(x, Q^2)$, the results are shown at $Q^2 = 2$ and 10 GeV^2 . One may also notice that the results of $F_2^{\text{EM}}(x, Q^2)$ are consistent with the corresponding phenomenological parameterization [596].

13.6 Sum Rules in DIS

The deep inelastic cross sections for the charged lepton–nucleon scattering or (anti)neutrino–nucleon scattering are described in terms of nucleon structure functions, which depend upon the momentum distribution of these quarks and gluons. Using the explicit expressions for structure functions, one can obtain certain relations. These relations are better known as parton model sum rules. Using the theory of strong interactions (QCD), the naive parton model and its predictions for the values of the sum rules are modified. At high energies (large momentum transfer squared), the coupling strength in QCD becomes small and perturbation theory can be used. In this regime, corrections to the sum rules can be expressed as a power series expansion in the strong coupling constant $\alpha_s(Q^2)$. At lower values of Q^2 , non-perturbative corrections enter and can be expressed as a power series in $1/Q^2$.

13.6.1 Adler sum rule

The Adler sum rule measures the validity of isospin symmetry in DIS, therefore, it is also known as the isospin sum rule. It deals with the measurements of the weak structure function $F_2^{\text{WI}}(x, Q^2)$. It is defined as:

$$\begin{aligned} S_A &= \int_0^1 \frac{dx}{x} [F_2^{\bar{\nu}p}(x) - F_2^{\nu p}(x)] \\ &= \int_0^1 \frac{dx}{x} 2x [(u(x) - \bar{u}(x)) - (d(x) - \bar{d}(x)) + (c(x) - \bar{c}(x)) - (s(x) - \bar{s}(x))]. \end{aligned}$$

Neglecting c and s quark PDFs,

$$S_A = \int_0^1 \frac{dx}{x} 2x [(u(x) - \bar{u}(x)) - (d(x) - \bar{d}(x))] = 2 = 4I_3.$$

Alternatively, one may write this sum rule in the following forms

$$\left. \begin{aligned} \int_0^1 \frac{dx}{x} [F_2^{\nu n}(x) - F_2^{\nu p}(x)] &= 2, & \int_0^1 \frac{dx}{x} [F_2^{\nu n}(x) - F_2^{\bar{\nu}n}(x)] &= 2, \\ \int_0^1 \frac{dx}{x} [F_2^{\bar{\nu}p}(x) - F_2^{\nu p}(x)] &= 2, & \int_0^1 \frac{dx}{x} [F_2^{\bar{\nu}p}(x) - F_2^{\bar{\nu}n}(x)] &= 2. \end{aligned} \right\} \quad (13.113)$$

The Adler sum rule [597] predicts the difference between the quark densities of the neutron and the proton integrated over x . At the leading order:

$$\int_0^1 (F_2^{\nu n}(x) - F_2^{\nu p}(x)) \frac{dx}{x} = \int_0^1 2(u_v(x) - d_v(x)) dx = 2. \quad (13.114)$$

The WA25 [598, 599] group used the neutrino beam on neutron and proton targets and instead of S_A , measured \tilde{S}_A which is defined as

$$\begin{aligned} \tilde{S}_A &\equiv \int_0^1 dx \left[\frac{F_2^{W^+n}(x, Q^2) - F_2^{W^+p}(x, Q^2)}{2x} \right] \\ &= \int_0^1 dx \left[u_v^p(x) - d_v^p(x) - \delta \bar{u}(x) - \delta \bar{d}(x) \right] \\ &= S_A - \int_0^1 dx \left[\delta \bar{u}(x) + \delta \bar{d}(x) \right], \end{aligned} \quad (13.115)$$

where $\bar{d}^n(x) \equiv \bar{u}^p(x) - \delta \bar{u}(x)$ and $\bar{u}^n(x) \equiv \bar{d}^p(x) - \delta \bar{d}(x)$ are the charge symmetry violating parton distribution functions for antiquarks. If $\delta \bar{u}(x)$ and $\delta \bar{d}(x)$ vanish, then the charge symmetry is exact. Moreover, this sum rule is supported by the existing neutrino–nucleon DIS data, which shows no significant Q^2 variation in the range $2 \text{ GeV}^2 < Q^2 < 30 \text{ GeV}^2$ and gives $S_A^{\text{exp}} = 2.02 \pm 0.40$ [599]. However, the error bars are large and DIS $\nu_l - N$ experiments with better precision are required to reduce errors. The experimental results from WA25 [598, 599] for the Adler sum rule shown in Figure 13.30 are in good agreement with the theoretical predictions.

13.6.2 Gross–Llewellyn Smith sum rule

The Gross–Llewellyn Smith (GLS) sum rule is defined for an isoscalar nucleon target ' N ' and a symmetric sea as

$$\begin{aligned} S_{GLS} = \int_0^1 dx F_3^{\nu N}(x) &= \int_0^1 dx \frac{1}{2} \left[F_3^{\nu p}(x) + F_3^{\nu n}(x) \right] \\ &= \int_0^1 dx \left[u(x) - \bar{u}(x) + d(x) - \bar{d}(x) + 2s(x) - 2\bar{s}(x) \right]. \end{aligned}$$

Neglecting sea quarks,

$$\int_0^1 dx F_3^{\nu N}(x) = \int_0^1 dx \left[u(x) - \bar{u}(x) + d(x) - \bar{d}(x) \right] = 3. \quad (13.116)$$

Using this sum rule, one may measure the baryon number and strangeness of the nucleon. Therefore, it is sometimes called the Baryon sum rule. One may also write:

$$\left. \begin{aligned} \int_0^1 \frac{dx}{x} x \left[F_3^{\nu p}(x) + F_3^{\bar{\nu} p}(x) \right] &= 6, & \int_0^1 \frac{dx}{x} x \left[F_3^{\nu p}(x) + F_3^{\nu n}(x) \right] &= 6, \\ \int_0^1 \frac{dx}{x} x \left[F_3^{\bar{\nu} p}(x) + F_3^{\bar{\nu} n}(x) \right] &= 6, & \int_0^1 \frac{dx}{x} x \left[F_3^{\nu n}(x) - F_3^{\bar{\nu} n}(x) \right] &= 6. \end{aligned} \right\}$$

The GLS sum rule gives the QCD expectation for the integral of the valence quark densities. To the leading order in perturbative QCD, the integral $\int \frac{dx}{x} [xF_3(x)]$ is the number of valence

quarks in the proton and should be equal to three [600]. QCD corrections to this integral result in a dependence on α_s [601]:

$$\int_0^1 x F_3(x, Q^2) \frac{dx}{x} = 3 \left(1 - \frac{\alpha_s}{\pi} - a(n_f) \left(\frac{\alpha_s}{\pi} \right)^2 - b(n_f) \left(\frac{\alpha_s}{\pi} \right)^3 \right), \quad (13.117)$$

where a and b are known functions of the number of quark flavors n_f which contribute to scattering at a given x and Q^2 . This is one of the few QCD predictions that are available to order α_s^3 . The world average is

$$\int_0^1 F_3(x) dx = 2.64 \pm 0.06,$$

which is consistent with the NNLO evaluation of Eq. (13.117) with $\Lambda = 250 \pm 50$ MeV.

13.7 Quark–hadron (QH) Duality

QCD is a theory which describes strong interactions in terms of quarks and gluons with remarkable features of asymptotic freedom at high energies (E_l) and momentum transfer squared (Q^2) and confinement at low energies and momentum transfer. At low E_l and Q^2 , the effective degrees of freedom to describe strong interactions are mesons and nucleons using effective Lagrangian; while at high E_l and Q^2 , the quark and gluon degrees of freedom are used to describe the strong interactions using perturbative QCD. In the case of scattering processes

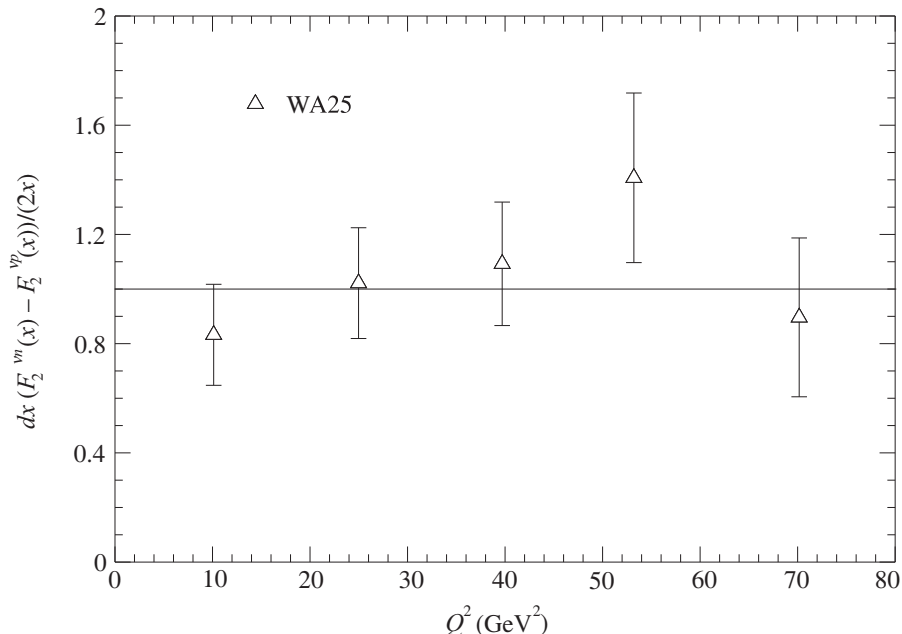


Figure 13.30 Experimental observations [598, 599] for the Adler sum rule.

induced by charged leptons and (anti)neutrino on nucleons, the inclusive cross sections at low energies are expressed in terms of structure functions corresponding to excitations of various nucleon resonances like Δ , N^* , etc. (Chapter 11, Table 11.3), lying in the first or higher resonance region. On the other hand, at high energies and Q^2 , the inclusive cross sections are expressed in terms of the structure functions corresponding to the deep inelastic scattering processes from quarks and gluons. In the intermediate energy region corresponding to the transition between resonance excitations and DIS, we are yet to find a method best suited to describe the inclusive charged lepton or (anti)neutrino scattering processes. Using the kinematical cuts in the $Q^2 - \nu$ plane (Figure 13.31), one may understand the regions like elastic ($W = M$), inelastic ($M \leq W \leq 2 \text{ GeV}$), DIS ($Q^2 > 1 \text{ GeV}^2$, $W > 2 \text{ GeV}$), soft DIS ($Q^2 < 1 \text{ GeV}^2$, $W > 2 \text{ GeV}$), and the shallow inelastic scattering (SIS) ($W < 2 \text{ GeV}$) regions. In order to emphasize the energy dependence of different scattering processes, in Figure 13.31 the variation of $Q^2 - \nu$ plane is shown at $E_\nu = 3 \text{ GeV}$ (left panel) and $E_\nu = 7 \text{ GeV}$ (right panel). As one moves away from the higher W region, where DIS (that deals with the quarks and gluons) is the dominant process to the region of SIS (resonant+nonresonant processes having hadrons as a degree of freedom). Presently, there is no sharp kinematic boundary to distinguish these two regions. In literature, $Q^2 \geq 1 \text{ GeV}^2$ has been chosen as the lower limit required for particles to be interacting with the quarks and gluonic degrees of freedom; a kinematic constraint of $W \geq 2 \text{ GeV}$ is also applied to safely describe the DIS region. Moreover, the kinematic region of $Q^2 \leq 1 \text{ GeV}^2$, where nonperturbative QCD must be taken into serious consideration, is yet to be explored. To understand this transition region, the phenomenon of quark–hadron duality comes into play; this duality basically connects the inclusive production processes in the two regions.

Historically, the concept of what was to become ‘duality’ began in the 1960s with the total pion–proton cross sections being compared with the Regge fit to higher energy data. It was concluded that low-energy hadronic cross sections, on an average, could be explained in terms of high-energy behavior. In the 1970s, Poggio, Quinn, and Weinberg [602] suggested that higher energy inclusive hadronic cross sections, appropriately averaged over an energy range, should approximately coincide with the cross sections calculated using quark–gluon perturbation theory. This directly implied that the physics of quarks and gluons could describe the physics of hadrons.

In 1970, Bloom and Gilman [603] defined duality by comparing the structure functions obtained from inclusive electron–nucleon scattering with the resonance production in similar experiments and the observation that the average over resonances is approximately equal to the leading twist contribution measured in the DIS region. This seems to be valid in each resonance region individually as well as in the entire resonance region when the structure functions are summed over higher resonances. For example, in Figure 13.32, the results of proton structure function F_2^p from SLAC and the Jefferson Lab in the resonance region for $0.06 < Q^2 < 3.30 \text{ GeV}^2$ are shown. The solid curve is a fit to deep inelastic scattering data at 5 GeV^2 . The figure is taken from Ref. [604]. From the figure, it may be observed that the DIS scaling curve extrapolated down into the resonance region passes through the average of the ‘peaks and valleys’ of the resonant structure. In this picture, the resonances

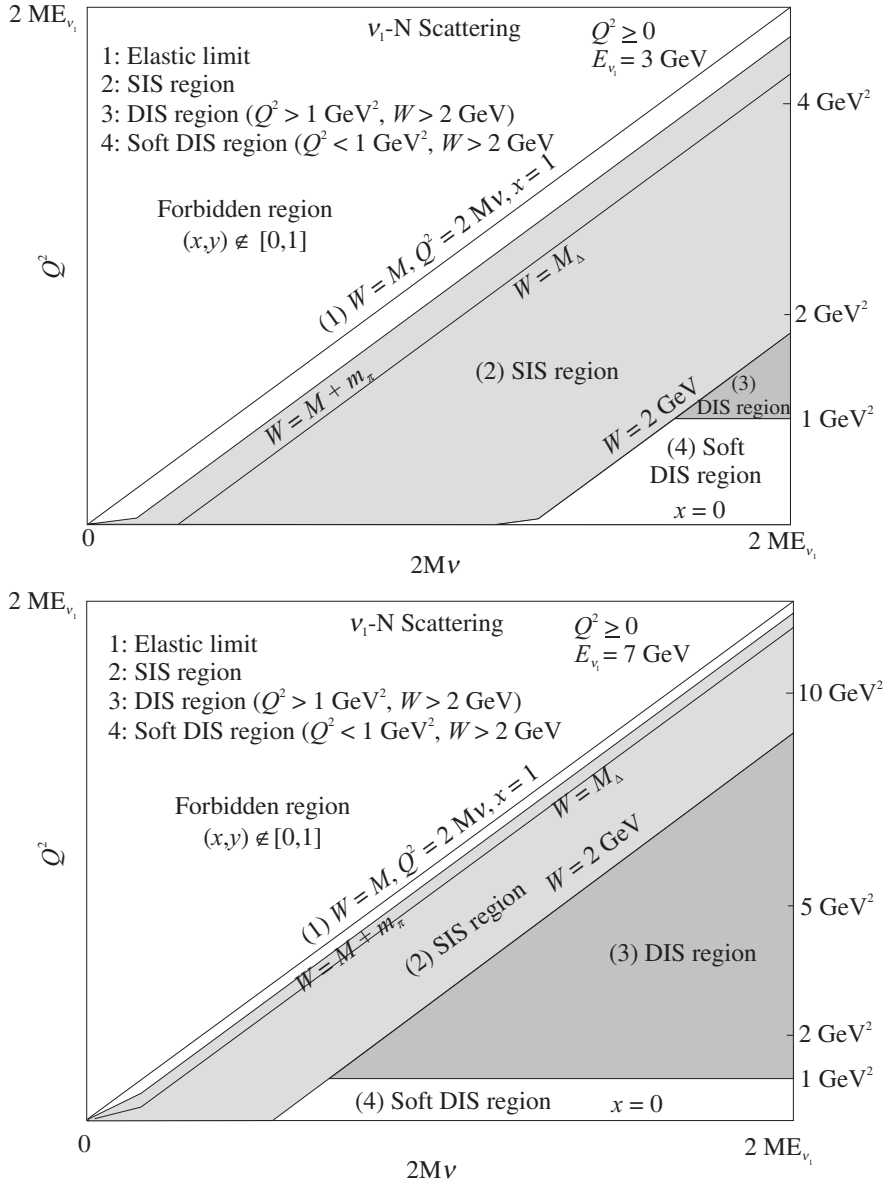


Figure 13.31 Allowed kinematical region for $\nu_l - N$ scattering in the $Q^2 - \nu$ plane for $E_\nu = 3$ GeV (left panel) and $E_\nu = 7$ GeV (right panel) for $Q^2 \geq 0$. Invariant mass square is defined as $W^2 = M^2 + 2M\nu - Q^2$ and the elastic limit is $x = \frac{Q^2}{2M\nu} = 1$. The forbidden region in terms of x and $y = \frac{\nu}{E_\nu} = \frac{(E_\nu - E_l)}{E_\nu}$ is defined as $x, y \notin [0, 1]$. The SIS region has been defined as the region for which $M + m_\pi \leq W \leq 2 \text{ GeV}$ and $Q^2 \geq 0$; the DIS region is defined as the region for which $Q^2 \geq 1 \text{ GeV}^2$ and $W \geq 2 \text{ GeV}$; and soft DIS region is defined as $Q^2 < 1 \text{ GeV}^2$ and $W \geq 2 \text{ GeV}$ (also part of SIS). Notice the unshaded band ($M < W < M + m_\pi$), where we do not expect anything from $\nu_l - N$ scattering; this region becomes important when the scattering takes place with a bound nucleon giving rise to an additional nuclear effect known as the multinucleon correlation effect.

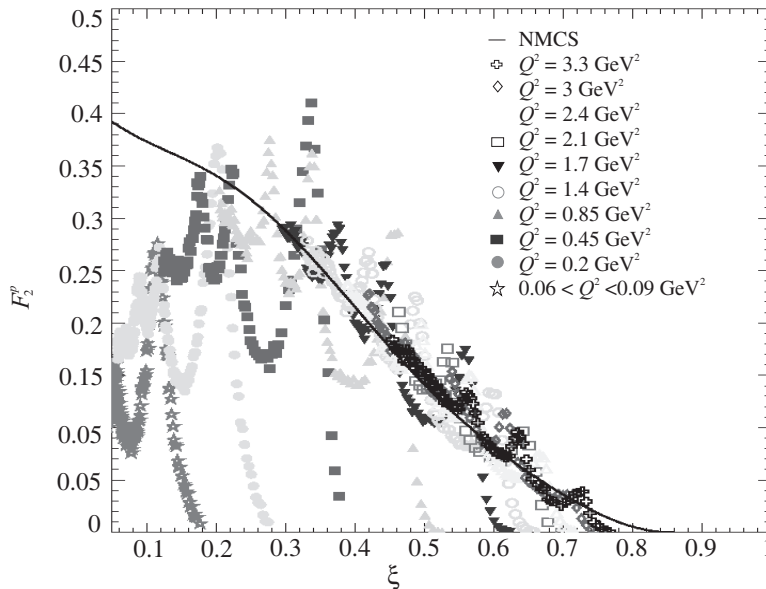


Figure 13.32 F_2^p structure function data on protons from SLAC and Jefferson Lab in the resonance region for $0.06 < Q^2 < 3.30 \text{ GeV}^2$. The solid curve is a fit to deep inelastic data at 5 GeV^2 . The figure is taken from Ref. [604].

can then be considered as a continuing part of the behavior observed in DIS. This would suggest that there is a connection between the behavior of resonances and QCD; perhaps even a common origin in terms of a point-like structure for both resonance and DIS interactions. Along this line, it has been conjectured that there may exist two component duality, where the resonance contribution and background contribution to the structure functions in the resonance excitation region correspond, respectively, to the valence quarks and the sea quarks contribution in structure functions in the DIS region [604]. However, these observations have to be verified by model calculations as well as by experimental data when they become available with higher precision. Currently, the observation of duality in charged lepton scattering has the following main features [605]:

- the resonance region data oscillate around the scaling DIS curve.
- the resonance data are on an average equivalent to the DIS curve.
- the resonance region data move toward the DIS curve with increase in Q^2 .

As more data with better precision become available on inclusive lepton scattering from nucleons and nuclei, a verification of QH duality with sufficient accuracy will provide a way to describe lepton–nucleon and lepton–nucleus scattering over the entire SIS region. Significantly, if duality does hold for neutrino nucleon interactions, it would be possible to extrapolate the better-known neutrino DIS structure into the SIS region and give an indication of how well current event simulators, the various Monte Carlo neutrino event generator being used in the neutrino oscillation analyses (like GENIE [606], NEUT [607] etc.) model the SIS region. An initial anomaly to note is that in current Monte Carlo (MC) event simulators/generators, ‘DIS’

is defined as ‘anything but QE and RES’, instead of the usually expressed kinematic condition on the effective hadronic mass such as $W > 2 \text{ GeV}$ with $Q^2 > 1 \text{ GeV}^2$. Notice moreover that such an MC generator definition of ‘DIS’ contains non-resonant pion production as well as a contribution from the kinematical region $Q^2 < 1 \text{ GeV}^2$ across the W region which is certainly outside of the applicability of the genuine DIS formalism and consequently, perturbative QCD. Thus, the MC definition of DIS also contains what we define as the SIS region [608].

This can be understood by looking at Figure 13.33, in which a full spectrum of different processes is shown [609]; the spectrum was obtained using the AGKY hadronization model [610]. The hadronization model has been adopted by the Monte Carlo generators such as GENIE MC used by current neutrino experiments. The detailed description of the hadronization model is beyond the scope of this book.

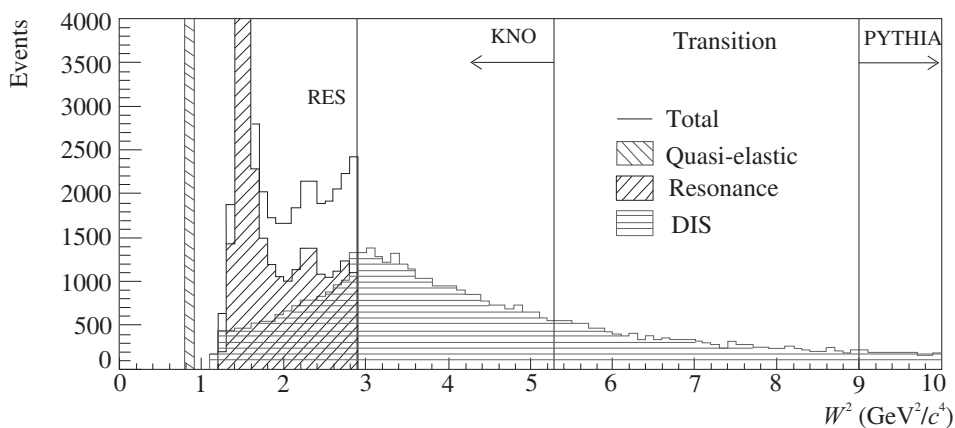


Figure 13.33 W^2 distribution of ν_μ -water target interactions in GENIE showing the quasi-elastic scattering, the resonance interactions, and the DIS region. The W distribution is further split into the three regions, KNO scaling-based model only region, PYTHIA only region, and the transition between the two regions used in the AGKY model [609].

In view of the extensive, precise experimental data on cross section and structure functions now available from JLab [611, 612, 613, 614], in a wide range of the kinematic region of electron–nucleon scattering and availability of electron DIS data from SLAC, EMC, NMC, and JLab in recent times, there is a wide international interest in studying quark–hadron duality. Phenomenological information on duality has also been accumulating for electron induced reaction channels [604]. The need for understanding (anti)neutrino–nucleon scattering cross sections in the transition region of $E_\nu \sim 1.5\text{--}3 \text{ GeV}$, has also generated considerable interest in studying QH duality in the weak sector, where it has been observed in the neutral current(NC) sector through the observation of parity violating asymmetry in the scattering of polarized electron from proton and deuteron targets at JLab [614]. However, for neutrino–nucleon scattering, there is lack of experimental data and few studies are available concerning duality in the weak sector [484, 615, 605, 616, 617, 618].

The validity of quark–hadron duality in the CC and NC sectors of weak interaction will provide a way to obtain (anti)neutrino–nucleon scattering cross sections in the transition region, where either the use of effective Lagrangian or the quark–parton description is not adequate.

QH duality will facilitate a model to obtain (anti)neutrino–nucleon cross sections in the entire energy region, which can be used in various MC neutrino event generators. This will be of interest to all neutrino oscillation experiments being done around the world in the few GeV energy region [619, 620, 621].

In the next sections, some of the experimental and theoretical results, which can illustrate the physical meaning of quark–hadron duality in the electromagnetic (Section 13.8) and weak (Section 13.9) interaction processes have been discussed.

13.8 Duality in Charged Lepton–nucleon Scattering

The differential cross section for the inclusive charged lepton scattering from nucleons in the DIS region is given in terms of structure functions $W_{iN}(\nu, Q^2)$, ($i = 1, 2$), which in the limits of high energy transfer and momentum transfer squared, are described in terms of the dimensionless structure functions $F_{1N}(x, Q^2)$ and $F_{2N}(x, Q^2)$:

$$F_{1N}(x, Q^2) = MW_{1N}(\nu, Q^2), \quad (13.118)$$

$$F_{2N}(x, Q^2) = \nu W_{2N}(\nu, Q^2). \quad (13.119)$$

In the resonance region, the inclusive cross section discussed in Chapters 11 and 12 is written as a coherent or incoherent sum of individual contributions from the resonance excitations R ($= \Delta, N^*$, etc.). This is diagrammatically shown in Figure 13.34. The expression of the cross section may be written as:

$$\frac{d^2\sigma}{d\Omega'_l dE'_l} = \frac{|\vec{k}'|^2 \alpha^2}{2Q^4} \frac{A(p')}{\sqrt{(k \cdot p)^2 - m_l^2 M_R^2}} L_{\mu\nu} W_R^{\mu\nu}, \quad (13.120)$$

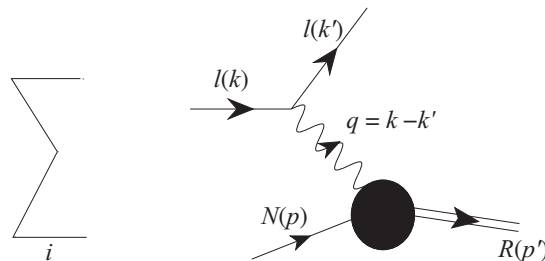


Figure 13.34 Diagrammatic representation of resonance excitations for $l + N \rightarrow l + R$.

where $L_{\mu\nu}$ is the leptonic tensor (as given in Eqs. (13.4) and (13.60)) and $W_R^{\mu\nu}$ is the hadronic tensor corresponding to the excitation of resonance R and is schematically given as

$$W_R^{\mu\nu} = \sum \sum \langle R(p') | J^\mu | N(p) \rangle^* \langle R(p') | J^\nu | N(p) \rangle, \quad (13.121)$$

$$A(p') = \frac{\sqrt{p'^2}}{\pi} \frac{\Gamma(p')}{(p'^2 - M_R^2)^2 + p'^2 \Gamma^2(p')}. \quad (13.122)$$

Here $\Gamma(p')$ is the momentum dependent width and M_R is the Breit–Wigner mass of the resonance. $\langle R(p') | J^\mu | N(p) \rangle$ corresponds to the transition matrix element for the transition $N(p) \rightarrow R(p')$ induced by the current J_μ . In the case of electromagnetic interaction, $l = e, \mu$, and J^μ has only the vector contribution.

As discussed in Chapters 11 and 12, the transition matrix element of hadronic current is characterized by various transition form factors $F_i^{pR}(Q^2)$ and $F_i^{nR}(Q^2)$ for proton and neutron targets depending upon the spin of the excited resonance $R(p')$. The form factors $F_i^{pR,nR}(Q^2)$ are derived from helicity amplitudes extracted from real and virtual photon scattering experiments. These form factors then describe the structure functions in the resonance region corresponding to each resonance excitations. In the case of excitations of more than one resonance, the sum in Fig. 13.34 can be done coherently or incoherently.

Once the structure functions are defined for the DIS and resonance region, $F_{i=1-3}^R(x, Q^2)$ are theoretically calculated assuming some parameterization of quark PDFs [622]. They are also determined experimentally (in nucleon as well as nuclear targets) by analyzing the data in the two regions which are available from various experiments performed at JLab, SLAC, EMC, NMC corresponding to the various regions of Q^2 and W . For a given Q^2 , x averaging is obtained over similar kinematic regions of W for each of them as follows:

$$\begin{aligned}\bar{F}_i^R(\Delta x, Q^2) &= \int_{x_{\min}}^{x_{\max}} dx F_i^R(x, Q^2) dx, \\ \bar{F}_i^{DIS}(\Delta x, Q^2) &= \int_{x_{\min}}^{x_{\max}} dx F_i^{DIS}(x, Q^2) dx, \\ \bar{F}_i^{exp}(\Delta x, Q^2) &= \int_{x_{\min}}^{x_{\max}} dx F_i^{exp}(x, Q^2) dx,\end{aligned}\tag{13.123}$$

where $i = 1, 2$ and x_{\min} and x_{\max} would correspond to W_{\min} and W_{\max} relevant for each resonance or DIS region. In some cases, variables other than x have also been used. For example, Bloom and Gilman [603] used $\omega' = \frac{2M\nu + M^2}{Q^2} = 1 + \frac{W^2}{Q^2} = \omega + \frac{M^2}{Q^2}$, while others have used the Nachtmann variable ξ [623]. The advantage with ξ is that it takes care of the TMC effect.

The degree to which duality is valid can be quantified by considering the ratio of integrals of the resonance and DIS structure functions at leading twist (LT). For example, Lalakulich et al. [484] have studied this ratio by defining

$$I_i(Q^2) = \frac{\int_{\xi_{\min}}^{\xi_{\max}} d\xi F_i^R(\xi, Q^2)}{\int_{\xi_{\min}}^{\xi_{\max}} d\xi F_i^{DIS}(\xi, Q^2)},\tag{13.124}$$

where $i = 1, 2$, and the integration limits correspond to $\xi_{\min} = \xi(W = 1.6 \text{ GeV}, Q^2)$ and $\xi_{\max} = \xi(W = 1.1 \text{ GeV}, Q^2)$. If the results are closer to unity, it would mean that the duality holds good. The authors [615] have obtained isoscalar nucleon structure function $F_2^{eN} = (F_2^{ep} + F_2^{en})/2$, calculated as a sum of electroproduced resonances. In Figure 13.35, results for F_2^{eN} at several values of Q^2 (from 0.2 to 2 GeV^2) have been presented as a function

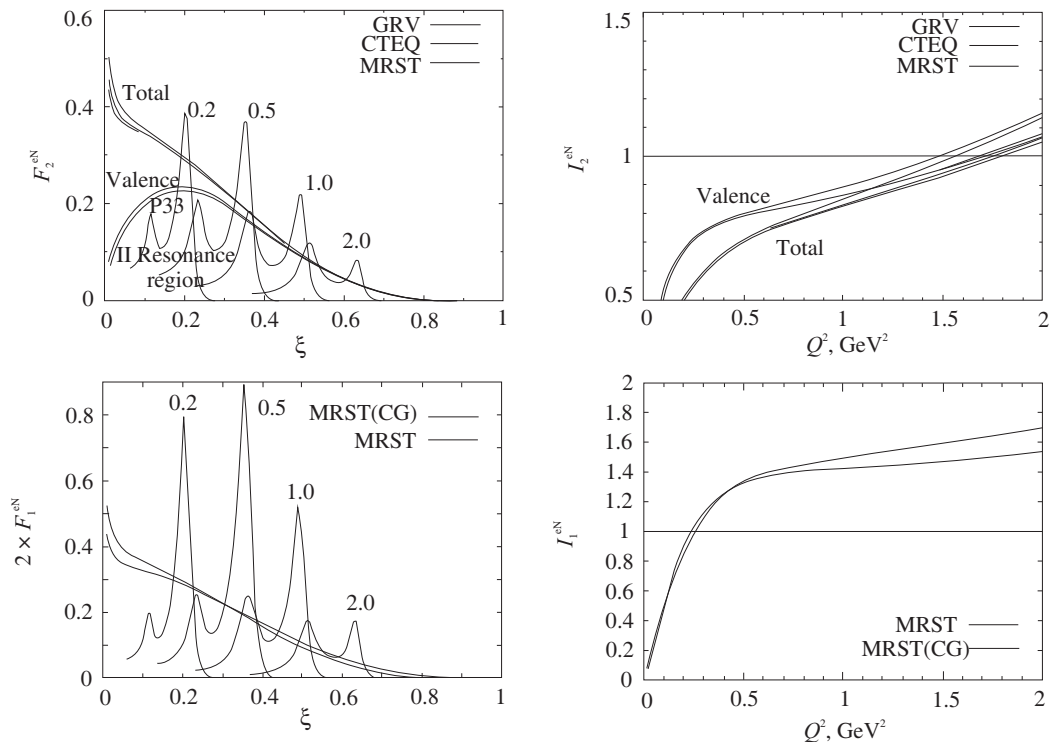


Figure 13.35 Top left panel: Duality for the isoscalar nucleon F_2^{eN} structure function. F_2^{eN} vs. ξ , for $Q^2 = 0.2, 0.5, 1$ and 2 GeV^2 , compared with several leading twist parameterizations [624, 625, 626] at $Q^2 = 10 \text{ GeV}^2$. Top right panel: Ratio I_2^{eN} of the integrated F_2^{eN} in the resonance region to the leading twist functions (valence and total). Bottom left panel: Duality for the isoscalar nucleon $2xF_1^{eN}$ structure function vs. ξ . The results are compared with the MRST parameterization [626] at $Q^2 = 10 \text{ GeV}^2$, using F_L and F_2 (dotted) and the Callan–Gross (CG) relation, $F_2 = 2xF_1$ (dot-dashed). Bottom right panel: Ratio I_1^{eN} of the integrated $2xF_1^{eN}$ in the resonance region to the leading twist function [626]. This figure is taken from Ref. [615].

of the Nachtmann variable ξ [615]. $P_{33}(1232)$ (Δ) has the maximum contribution at the largest value of ξ that may be realized by looking at the prominent peaks, followed by peaks at smaller ξ , corresponding to the second resonance region, where the $S_{11}(1535)$ and $D_{13}(1520)$ resonances dominate. It has been found that the contribution from the $P_{11}(1440)$ resonance is small. Furthermore, it may be observed from these figures that with the increase in Q^2 , the peaks in the resonance region decrease in height and move to larger ξ . In this figure (right panel), the results for the ratio I_2^{eN} has also been presented. It has been found [615] that the integrated resonance contribution is smaller at low Q^2 , but increases with the increase in the value of Q^2 . It may also be observed that for the results obtained with the valence-only structure function, the ratio is within $\sim 20\%$ of unity over a larger range, $Q^2 \gtrsim 0.5 \text{ GeV}^2$.

Figure 13.35 (bottom panel) shows the isoscalar nucleon structure function $2xF_1^{eN}$, calculated for the four resonances ($P_{33}(1232)$, $S_{11}(1535)$, $D_{13}(1520)$, and $P_{11}(1440)$). The results are compared with the leading twist parameterization from Ref. [626] at $Q^2 = 10 \text{ GeV}^2$, for the two different cases (i) using the Callan–Gross relation $F_2 = 2xF_1$, and (ii) in terms of F_L

and F_2 [615]. It may be noticed that the difference between the two curves is relatively small at $Q^2 = 10 \text{ GeV}^2$, and with the increase in Q^2 , the resonance structure function $2xF_1^{eN}$ is seen to slide along the leading twist curve. However, the average sits slightly higher than the leading twist curve. This can be quantified by considering the ratio I_1^{eN} defined in Eq. (13.124), which has been plotted in Figure 13.35 (right panel) [615]. It may also be observed that for most of the range of $Q^2 \gtrsim 0.5 \text{ GeV}^2$, the ratio is some 30 – 50% above unity, which indicates that either additional resonances are required or better understanding of duality is needed.

13.9 Duality in Neutrino–nucleon Scattering

In the weak sector, the quark-hadron duality has been shown to work in the neutral current (NC) sector of polarized electron–nucleon scattering, as observed in the parity violation (PV) asymmetry of electron from protons and deuterons [614]. There has been no experimental study of quark–hadron duality in CC and NC sectors of neutrino and antineutrino interactions. This is mainly due to the lack of (anti)neutrino scattering data on resonance production from nucleons and nuclei. However, the cross section measurements from MINERvA, NOvA, and the planned DUNE experiment, may be useful to test quark–hadron duality in nucleon and nucleus scattering with the (anti)neutrino. On the other hand, there are some theoretical studies to test quark–hadron duality in neutrino scattering, where $\bar{F}_i^R(Q^2)$ and $\bar{F}_i^{DIS}(Q^2)$ have been calculated in certain theoretical models and compared with each other [484, 615, 616, 617, 618]. If theoretical calculations validate the quark–hadron duality, it will provide a powerful method to model the (anti)neutrino–nucleus cross sections in the transition region. This is highly desirable as it will provide a method to calculate (anti)neutrino nucleus cross sections in the entire region of $\nu(\bar{\nu})$ energies relevant for ν -oscillation experiments [627, 628, 629].

In the case of weak neutral current $l = e, \mu, \nu_e, \nu_\mu, \bar{\nu}_e, \bar{\nu}_\mu$ as well as the weak charged current $l = (\nu_e, e^-), (\nu_\mu, \mu^-), (\bar{\nu}_e, e^+), (\bar{\nu}_\mu, \mu^+)$ interactions, the weak interaction vertex has both the vector and axial vector contributions. We have seen in Chapter 12 that for weak interaction induced charged current reaction $\nu_\mu p \rightarrow \mu^- \Delta^{++}$, only isospin 3/2 resonances are excited (mainly $P_{33}(1232)$). Due to isospin symmetry constraints, the neutrino–proton structure functions ($F_2^{\nu p}, 2xF_1^{\nu p}$ and $xF_3^{\nu p}$) for these resonances are three times larger than the neutrino–neutron structure functions. Due to the dominance of Δ^{++} , the resonance structure functions are significantly larger than the DIS structure functions, $F_i^{\nu p(\text{res})} > F_i^{\nu p(\text{DIS})}$, and quark–hadron duality is violated for the interaction taking place with a proton target [615].

In the case of neutrino–neutron scattering, in addition to the dominant contribution from isospin $I = 3/2$ resonances, there is non-negligible contribution from $I = 1/2$ resonances. For example, the study made by Lalakulich et al. [484, 615], observed that $I = 1/2$ resonances, viz., $P_{11}(1440)$, $D_{13}(1520)$ and $S_{11}(1535)$, contribute to the cross section albeit small as compared to the $P_{33}(1232)$ resonance. It has been found that the leading twist curve for the νn structure functions lies above the resonance structure functions, $F_i^{\nu n(\text{res})} < F_i^{\nu n(\text{DIS})}$, and, therefore, the quark–hadron duality does not hold even in the case of neutrino–neutron

scattering. However, there is need to consider the contribution from higher resonances before a conclusion is drawn (see Figure 13.36).

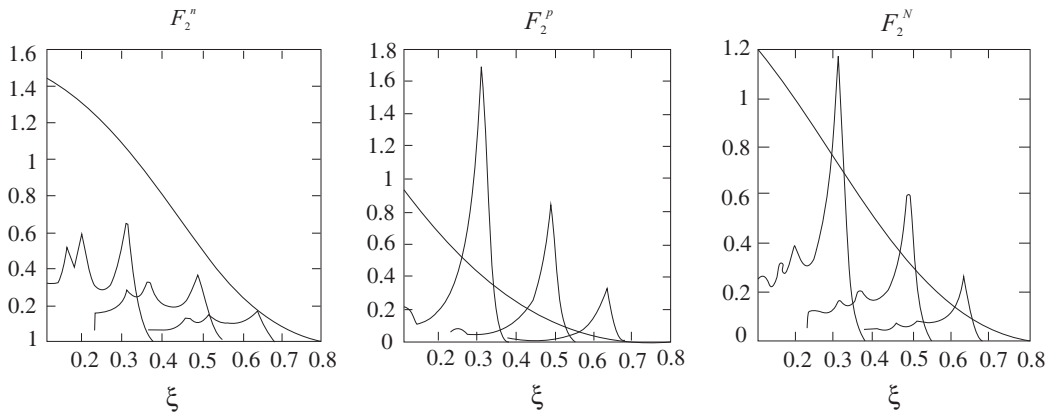


Figure 13.36 Figure from [616]: (upper) Comparison of the Rein–Sehgal F_2 structure functions vs. ξ for neutron, proton, and the isoscalar nucleon target at $Q^2 = 0.4, 1$ and 2 GeV^2 (left to right in each figure) with the appropriate DIS scaling functions at $Q^2 = 10 \text{ GeV}^2$.

In Figure 13.37, the results for the weak structure function $F_2^{\nu N}$ vs. ξ are presented for the neutrino–nucleon scattering at several values of Q^2 . It may be observed that $P_{33}(1232)$ resonance has the largest peak at each value of Q^2 . The next peak may be seen at lower ξ (larger W) which is dominated by the $D_{13}(1520)$ and $S_{11}(1535)$ resonances. With the increase in Q^2 , the contribution from $D_{13}(1520)$ and $S_{11}(1535)$ resonances become significant. These authors [484] have also obtained a theoretical curve for $F_2^{\nu N} = x(u + \bar{u} + d + \bar{d} + s + \bar{s})$, (extreme left panel) using GRV [624] and CTEQ [625] leading twist parton distributions at $Q^2 = 10 \text{ GeV}^2$. It may be noticed that like in the case of electron–nucleon scattering, here also with the increase in Q^2 , the resonances slide along the leading twist curve, which is required by duality. In this figure, the results for $2xF_1^{\nu N}$ vs. ξ (central panel) have also been shown. The leading twist functions correspond to the MRST parameterization [626] using the Callan–Gross

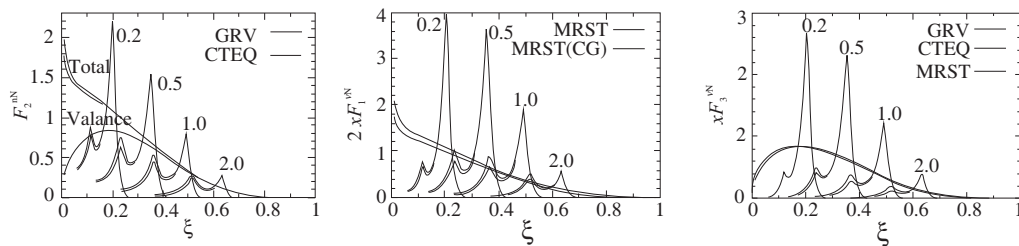


Figure 13.37 Duality for the neutrino–nucleon $F_2^{\nu N}$, $2xF_1^{\nu N}$ and $xF_3^{\nu N}$ structure functions in the resonance region at several Q^2 values, indicated against their spectra [615]. (Left) $F_2^{\nu N}$ vs. ξ . The results are compared with leading twist parameterizations [624, 625] (valence and total) at $Q^2 = 10 \text{ GeV}^2$. (Center) $2xF_1^{\nu N}$ vs. ξ . The results are compared with the exact expression in Eq. (13.46) (dotted) and Callan–Gross relation (dot-dashed). (Right) $xF_3^{\nu N}$ vs. ξ . The results are compared with several leading twist parameterizations [624, 625, 626].

relation in terms of F_L . It may be observed that the resonance contributions appear to lie above the leading twist curve for a wide range of ξ . The extreme right panel of this figure shows χF_3^{vN} vs. ξ . It has been found by Lalakulich et al. [484] that for the resonances considered in their work, the proton F_3^{vp} structure function is larger than the neutron F_3^{vn} structure function, whereas for deep inelastic scattering, the νn is larger.

Thus more work is required to understand duality in the weak sector. This is an emerging area of theoretical as well as experimental interest.